

Discovery of charge density wave in a kagome lattice antiferromagnet

<https://doi.org/10.1038/s41586-022-05034-z>

Received: 9 January 2022

Accepted: 28 June 2022

Published online: 14 September 2022

 Check for updates

Xiaokun Teng¹, Lebing Chen¹, Feng Ye², Elliott Rosenberg³, Zhaoyu Liu³, Jia-Xin Yin⁴, Yu-Xiao Jiang⁴, Ji Seop Oh^{1,5}, M. Zahid Hasan⁴, Kelly J. Neubauer¹, Bin Gao¹, Yaofeng Xie¹, Makoto Hashimoto⁶, Donghui Lu⁶, Chris Jozwiak⁷, Aaron Bostwick⁷, Eli Rotenberg⁷, Robert J. Birgeneau^{5,8}, Jiun-Haw Chu³, Ming Yi^{1✉} & Pengcheng Dai^{1✉}

A hallmark of strongly correlated quantum materials is the rich phase diagram resulting from competing and intertwined phases with nearly degenerate ground-state energies^{1,2}. A well-known example is the copper oxides, in which a charge density wave (CDW) is ordered well above and strongly coupled to the magnetic order to form spin-charge-separated stripes that compete with superconductivity^{1,2}. Recently, such rich phase diagrams have also been shown in correlated topological materials. In 2D kagome lattice metals consisting of corner-sharing triangles, the geometry of the lattice can produce flat bands with localized electrons^{3,4}, non-trivial topology^{5–7}, chiral magnetic order^{8,9}, superconductivity and CDW order^{10–15}. Although CDW has been found in weakly electron-correlated non-magnetic AV_3Sb_5 ($A = K, Rb, Cs$)^{10–15}, it has not yet been observed in correlated magnetic-ordered kagome lattice metals^{4,16–21}. Here we report the discovery of CDW in the antiferromagnetic (AFM) ordered phase of kagome lattice FeGe (refs. ^{16–19}). The CDW in FeGe occurs at wavevectors identical to that of AV_3Sb_5 (refs. ^{10–15}), enhances the AFM ordered moment and induces an emergent anomalous Hall effect^{22,23}. Our findings suggest that CDW in FeGe arises from the combination of electron-correlations-driven AFM order and van Hove singularities (vHSs)-driven instability possibly associated with a chiral flux phase^{24–28}, in stark contrast to strongly correlated copper oxides^{1,2} and nickelates^{29–31}, in which the CDW precedes or accompanies the magnetic order.

CDW is a state in which electronic charge density in a metal becomes spatially modulated and imposes a new lattice periodicity on a crystal, leading to the reorganization of the electronic bands of the parent phase³². For weakly electron-correlated AV_3Sb_5 (ref. ¹⁵), CDW can coexist and compete with superconductivity without magnetism. It is associated with an anomalous Hall effect (AHE)^{22,23} (Fig. 1), proposed to arise from Fermi surface nesting of vHSs between the M-L (Fig. 2a) and M-M (Fig. 2b) points of the Brillouin zone (BZ)^{33,34}, and may host a time-reversal-symmetry-breaking chiral flux phase of circulating currents^{24–28} (Fig. 1d). In strongly electron-correlated copper oxides^{1,2} and nickelates^{29–31}, CDW and associated lattice distortion always appear as a precursor to magnetism, onset at temperatures well above or simultaneously with the magnetic order. There is not yet an example of a coupled CDW and magnetic order in which the CDW appears at a temperature well below the magnetic ordering temperature.

In metals with kagome lattices (Fig. 1a), destructive phase interference of nearest-neighbour electronic hopping can induce flat electronic bands^{5–7}. When flat bands are near the Fermi level, E_F , strong electron correlations can induce magnetic order^{4,5}. Although magnetism in FeSn orders below $T_N \approx 365$ K with in-plane ferromagnetic

(FM) moments in each layer stacked antiferromagnetically along the c-axis^{20,21}, kagome lattice FeGe (Extended Data Tables 1–3) exhibits collinear A-type AFM order below $T_N \approx 410$ K (Fig. 1b) and becomes a c-axis double cone (canting) AFM structure below $T_{\text{Canting}} \approx 60$ K (refs. ^{18,19}).

Here we report the discovery of a short-range CDW inside the AFM phase of FeGe below $T_{\text{CDW}} \approx 100$ K at wavevectors (\mathbf{Q}_S) identical to that of AV_3Sb_5 (refs. ^{10–15}), from a combined study of magnetization (Fig. 1e,f,i and Extended Data Fig. 2), transport (Fig. 1g,h,j and Extended Data Fig. 3), neutron and X-ray scattering (Figs. 2 and 3a–h, Extended Data Figs. 1 and 4–8 and Extended Data Tables 1–4), scanning tunnelling microscopy (STM)⁷ (Fig. 3i,j and Extended Data Fig. 9a) and angle-resolved photoemission spectroscopy (ARPES; Fig. 4 and Extended Data Fig. 9b) experiments. We find that the CDW in FeGe enhances the moment of collinear AFM order (Fig. 1c) and induces an AHE similar to that of AV_3Sb_5 (refs. ^{22,23}) (Fig. 1k), consistent with a chiral flux phase of circulating currents^{24–28} (Fig. 1d). We also observe sets of vHSs near E_F in the electronic band structure separated by the \mathbf{Q}_S identified from neutron diffraction^{10–15,33,34}. Because AFM order in FeGe probably arises from electronic correlations of the flat electronic

¹Department of Physics and Astronomy, Rice University, Houston, TX, USA. ²Neutron Scattering Division, Oak Ridge National Laboratory, Oak Ridge, TN, USA. ³Department of Physics, University of Washington, Seattle, WA, USA. ⁴Laboratory for Topological Quantum Matter and Advanced Spectroscopy, Department of Physics, Princeton University, Princeton, NJ, USA. ⁵Department of Physics, University of California, Berkeley, Berkeley, CA, USA. ⁶Stanford Synchrotron Radiation Lightsource, SLAC National Accelerator Laboratory, Menlo Park, CA, USA. ⁷Advanced Light Source, Lawrence Berkeley National Laboratory, Berkeley, CA, USA. ⁸Materials Sciences Division, Lawrence Berkeley National Laboratory, Berkeley, CA, USA. [✉]e-mail: mingy@rice.edu; pdai@rice.edu

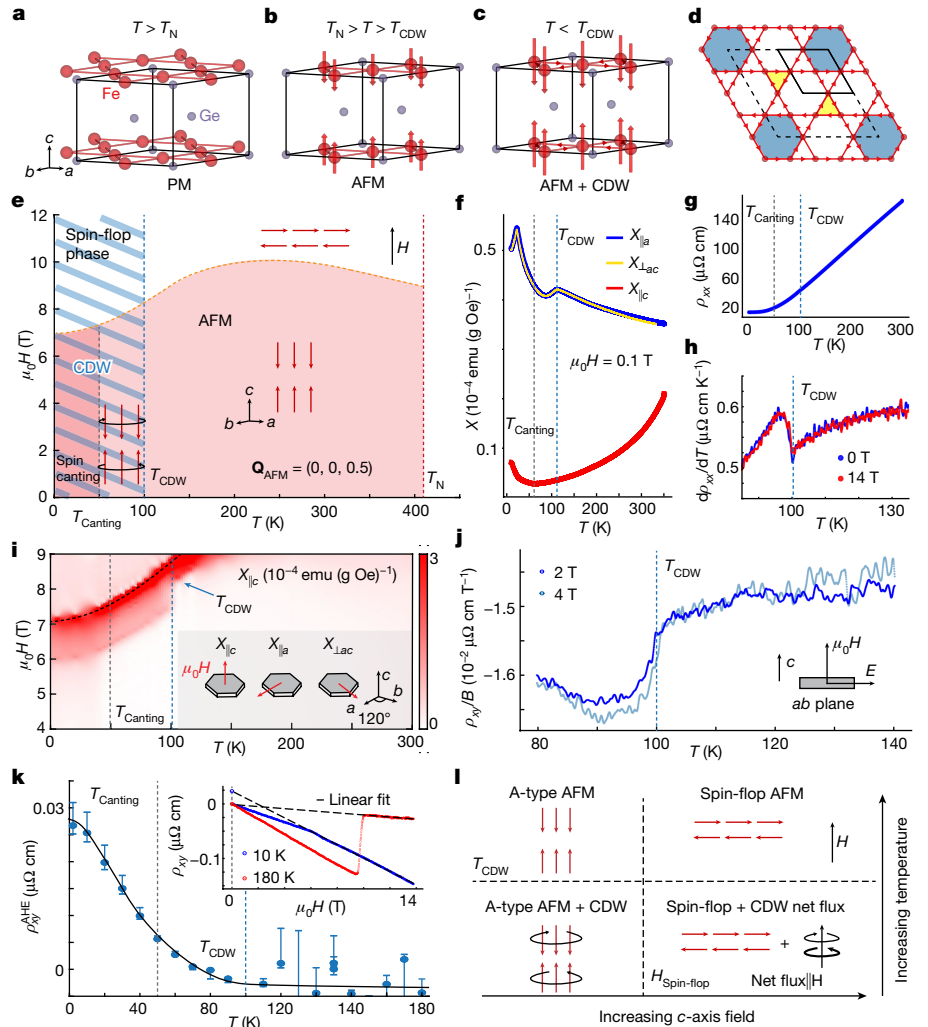


Fig. 1 | Crystal and magnetic structure, phase diagram, sample characterization and schematic of flux phase in FeGe. **a**, Crystal structure in paramagnetic (PM) phase ($T > T_N$). Unit cell is marked with solid grey lines. The Fe kagome layers are interleaved with Ge layers. **b**, Magnetic structure in temperature regime $T_N > T > T_{CDW}$. Spins are aligned in each Fe layer and anti-aligned across the layers. **c**, Magnetic structure in $T_{CDW} > T > T_{Canting}$. Moments are enhanced in the CDW state. Red arrows on Fe-Ge bonds indicate possible flux currents. **d**, A schematic of the in-plane flux phase. **e**, Temperature-field phase diagram of FeGe. Blue shaded area is the CDW state. **f**, Magnetic susceptibility of FeGe measured with a 0.1-T field. $\chi_{\perp ac}$ and $\chi_{\parallel a}$ are measured with the field in the ab plane and $\chi_{\parallel c}$ is measured along the c -axis (inset of **i**). There is a kink in $\chi_{\perp ac}$ and $\chi_{\parallel a}$ at T_{CDW} . **g**, **h**, Temperature dependence of in-plane resistivity ρ_{xx} and its derivative with respect to temperature. A kink is observed in **h** at T_{CDW} . **i**, Out-of-plane magnetic susceptibility at different fields and temperatures. Spin-flop transition temperature is marked with a dashed black line. There is a prominent onset that shows that spins are more easily flopped below T_{CDW} . **j**, Temperature dependence of Hall resistivity with in-plane electric field and magnetic field along the c -axis. A decrease in Hall resistivity is observed at T_{CDW} . **k**, Temperature dependence of ρ_{xy}^{AHE} (refs. ^{22,23}). It is extracted by taking the zero-field intercept of linear fitting at the spin-flop phase (see inset of **k**). The vertical error bars represent the estimated uncertainty in ρ_{xy}^{AHE} . **l**, Schematic of the interplay between spin-flop and flux phase in FeGe. Below T_{CDW} , the in-plane CDW net flux is enhanced selectively after the spin-flop transition.

bands near the Fermi level⁴, the CDW could be induced by the nesting of vHSs in the spin-polarized electronic bands below T_N .

Experimental data

Figure 1e shows temperature versus c -axis aligned magnetic-field-dependent phase diagram of FeGe as determined from our magnetic susceptibility (Fig. 1f,i and Extended Data Fig. 2) and neutron scattering (Figs. 2 and 3a–f) measurements. Below T_N and $T_{Canting}$, we confirm the A-type AFM order (Fig. 1b and Extended Data Fig. 8a–c) and canted AFM structure (Fig. 2c and Extended Data Fig. 8d,e), respectively^{18,19}. Temperature-dependent susceptibilities (Fig. 1f) for in-plane field parallel and perpendicular to the a -axis directions ($\chi_{\parallel a}$ and $\chi_{\perp ac}$) are identical and show a clear reduction around 100 K distinct from both T_N and $T_{Canting}$. Although temperature-dependent susceptibility along the c -axis

resistivity ρ_{xx} and its derivative with respect to temperature. A kink is observed in **h** at T_{CDW} . **i**, Out-of-plane magnetic susceptibility at different fields and temperatures. Spin-flop transition temperature is marked with a dashed black line. There is a prominent onset that shows that spins are more easily flopped below T_{CDW} . **j**, Temperature dependence of Hall resistivity with in-plane electric field and magnetic field along the c -axis. A decrease in Hall resistivity is observed at T_{CDW} . **k**, Temperature dependence of ρ_{xy}^{AHE} (refs. ^{22,23}). It is extracted by taking the zero-field intercept of linear fitting at the spin-flop phase (see inset of **k**). The vertical error bars represent the estimated uncertainty in ρ_{xy}^{AHE} . **l**, Schematic of the interplay between spin-flop and flux phase in FeGe. Below T_{CDW} , the in-plane CDW net flux is enhanced selectively after the spin-flop transition.

($\chi_{\parallel c}$) is consistent with the earlier work¹⁷, the 100-K feature in $\chi_{\parallel a}$ and $\chi_{\perp ac}$ has not been reported (Extended Data Fig. 2). Because we find no change in the magnetic structure across 100 K (Extended Data Fig. 8a–c), the reduction of susceptibility is consistent with gapping density of states at the Fermi level by the CDW. The in-plane resistivity (ρ_{xx}) exhibits a seemingly featureless metallic behaviour (Fig. 1g), yet its temperature derivative shows a clear kink at T_{CDW} (Fig. 1h). The ρ_{xx} absolute values change from 150 $\mu\Omega$ cm at 300 K to about 18 $\mu\Omega$ cm around 2 K, similar to that of FeSn (ref. ²⁰), but is much larger than the value of approximately 30 $\mu\Omega$ cm at 300 K for AV_3Sb_5 (ref. ¹⁰). Because the band renormalization factor in FeGe (Fig. 4) is larger than that for AV_3Sb_5 (ref. ¹⁰), the much larger resistivity of FeGe indicates that it is closer to the bad-metal regime with stronger electron correlations³⁵. The Hall resistivity (ρ_{xy}) also shows signatures at T_{CDW} (Fig. 1j). When a magnetic field ($B = \mu_0 H$) is applied along the c -axis, a spin-flop transition occurs

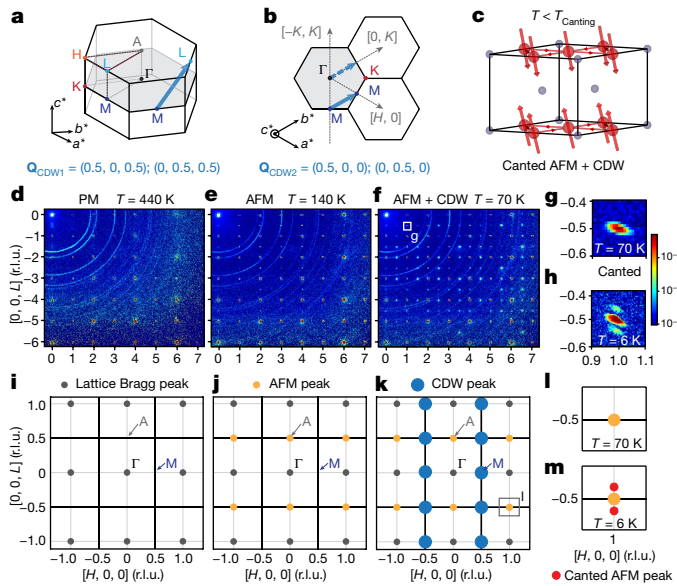


Fig. 2 | BZ, canted AFM structure, neutron diffraction data and schematic in the $[H, 0, L]$ plane. **a,b**, 3D and 2D BZ of FeGe, respectively. The high symmetry points are specified. CDW \mathbf{Q} s are marked using thick blue arrows. **c**, Canted AFM structure of FeGe below T_{Canting} . Flux currents in the CDW phase are marked with red arrows on in-plane Fe bonds. **d–h**, Neutron diffraction pattern of FeGe at indicated temperatures in the $[H, 0, L]$ plane. The intensity colour bar is in log scale. **d**, At 440 K, only lattice Bragg peaks at $(H, 0, L)$ ($H, L = 0, \pm 1, \pm 2, \dots$) are present. **e**, At 140 K, the system is in c -axis collinear AFM state, AFM peaks emerge at $\mathbf{Q}_{\text{AFM}} = (H, 0, L+0.5)$. **f**, At 70 K, CDW coexists with commensurate AFM order, extra CDW peaks appear at $\mathbf{Q}_{\text{CDW}1} = (H+0.5, 0, L+0.5)$ and $\mathbf{Q}_{\text{CDW}2} = (H+0.5, 0, L)$. There is also a weak non-magnetic peak at $(7, 0, -4.5)$, whose origin is unknown. The commensurate magnetic peak at $\mathbf{Q}_{\text{AFM}} = (1, 0, 0.5)$ is enlarged in **g**. Below (H, L) , satellite magnetic peaks emerge, as shown in **h**, indicating further modulation along the c -axis^{18,19}. The rings of scattering in **d–f** are from the aluminium sample holder. **i–k**, Schematic of the $[H, 0, L]$ plane reciprocal space maps in the PM phase, AFM phase and AFM + CDW phase. Lattice Bragg peaks, AFM peaks and CDW peaks are shown with grey, orange and blue dots, respectively. **l,m**, Enlarged magnetic peaks at 70 K and 6 K. Red dots indicate extra incommensurate magnetic peaks below T_{Canting} .

above a critical field, in which the c -axis-aligned moments are flopped to be parallel to the ab plane¹⁷ (Fig. 1e,i). Below the spin-flop transition, ρ_{xy} is linear in field (inset of Fig. 1k and Extended Data Fig. 3a,b), which allows us to extract the weak field Hall coefficient simply from ρ_{xy}/B (Fig. 1j). The temperature dependent ρ_{xy}/B decreases at 100 K, reminiscent of χ_{Lac} and χ_{AHE} (Fig. 1i and Extended Data Fig. 3c,e). At the spin-flop critical field, there is a sudden change of both the value and the slope of ρ_{xy} (inset of Fig. 1k and Extended Data Fig. 3a,b), which is a result of both change of the ordinary Hall coefficient resulting from the spin-flop and the contribution from the AHE, occurring at temperature below T_{CDW} . Although the initial definition of the AHE is the spontaneous Hall effect at zero field³⁶, recent studies have shown that the AHE can also arise in antiferromagnets, resulting from the field-induced magnetization and/or non-collinear spin structure³⁷. We extracted the anomalous Hall resistivity (ρ_{AHE}) by using the zero-field intercept of the linear fit of ρ_{xy} above the spin-flop field³⁷ (inset of Fig. 1k). Although the ρ_{AHE} fluctuates around zero above T_{CDW} , it gradually increases as the temperature decreases below T_{CDW} and saturates at a maximum value of $0.027 \mu\Omega \text{ cm}$, similar to that of AV_3Sb_5 ($0.04 \mu\Omega \text{ cm}$ at 5 K)^{22,23}. However, unlike AV_3Sb_5 , in which the AHE is seen as a highly non-linear Hall resistivity at low field (<2 T), there is no sign of AHE in FeGe in the low-field range. The fact that the effect of CDW on AHE can only be seen in the spin-flop state where Fe magnetization kicks in (Fig. 1k,l) strongly suggests a coupling between magnetism and CDW.

Next, we present neutron scattering results in the $[H, 0, L]$ scattering plane, as seen in the 3D (Fig. 2a) and in-plane 2D reciprocal space of FeGe (Fig. 2b). We start in the paramagnetic state, in which the raw data taken at 440 K in Fig. 2d show only nuclear Bragg peaks, as illustrated in Fig. 2i. On cooling to 140 K ($T_{\text{CDW}} < T < T_N$), a set of new magnetic Bragg peaks at $(H, 0, L+0.5)$ \mathbf{Q} s appear (Fig. 2e,j and Extended Data Fig. 4a–h). Refinements of the neutron diffraction data confirm the A -type AFM structure^{18,19} (Fig. 1b and Extended Data Fig. 8b). On further cooling to 70 K ($T > T_{\text{Canting}}$)^{18,19}, more peaks appear at $(H+0.5, 0, L)$, $(H+0.5, 0, L+0.5)$ (Fig. 2f,k and Extended Data Fig. 4i–m) and $(0, K+0.5, L)$, $(0, K+0.5, L+0.5)$ \mathbf{Q} s (Fig. 2f,k and Extended Data Figs. 4i–m and 7a–f). As these peaks persist to large \mathbf{Q} -positions (that is, at $(6.5, 0, -5.5)$), at which the Fe^{2+} magnetic form factor drops off substantially, they must be non-magnetic and associated with lattice distortions induced by a CDW (Fig. 2f,k, Extended Data Figs. 5, 6 and 8f,g and Extended Data Table 4). On further cooling to below T_{Canting} , more magnetic peaks develop along the L direction, as seen in Fig. 2g (70 K) and Fig. 2h (6 K), consistent with a magnetic structural modulation along the c -axis (Fig. 2l,m) and the canted AFM structure^{18,19} (Fig. 2c and Extended Data Fig. 8d,e).

Figure 3a,b shows the temperature dependence of the $(2.5, 0, 2)$ and $(3.5, 0, 1.5)$ CDW peaks across 100 K, respectively. They correspond to $L = 0$ and 0.5 along the c -axis, similar to that found in AV_3Sb_5 (refs. ^{10–15}). The scattering intensities at both \mathbf{Q} s increase simultaneously below about 100 K, but cannot be fitted with a standard second-order phase transition. Figure 3c,d shows \mathbf{Q} scans along the $[2.5, 0, L]$ and $[H, 0, 2]$ directions, respectively. The scattering is featureless at 140 K but becomes a well-defined peak centred at $(2.5, 0, 2)$ at 70 K. The peak profile can be best fit by a Lorentzian and is much broader than the instrumental resolution determined by the widths of the nearby nuclear and magnetic Bragg peaks (horizontal bars in Fig. 3c,d and Extended Data Fig. 4g–l). Fourier transform of the peak gives correlation lengths of roughly 33 Å along the in-plane and roughly 45 Å along the c -axis directions, therefore suggesting that this is a short-range order. Figure 3e shows the temperature dependence of the magnetic ordered moment square obtained by normalizing the integrated intensity of magnetic peak at $(2, 0, 0.5)$ to moment size squared obtained from refinements of single-crystal data at 140 K (Fig. 2e). As well as confirming T_N (refs. ^{18,19}) (Fig. 3e), we find an enhancement of the ordered magnetic moment below T_{CDW} (Fig. 3f), indicating a strong coupling of the magnetic order and CDW. Below about 60 K, incommensurate magnetic Bragg peaks from the canted AFM structure appear, accompanied by a reduction in the magnetic Bragg peak intensity at $(2, 0, 0.5)$ (Fig. 3f). For comparison, the CDW peak intensity does not change in the canted AFM phase (Fig. 3a,b). Therefore, although the CDW order clearly enhances the ordered moment of the collinear A -type AFM phase, the CDW intensity does not change on the formation of the canted AFM structure.

To demonstrate that the approximately 100 K structural superlattice modulation is indeed associated with a CDW transition, we carried out STM measurements on FeGe. Figure 3g shows the atomic lattice of the cryogenic cleaving surface of FeGe. Measuring the differential conductance spectrum that is proportional to the local density of states, we detect a pronounced suppression at the Fermi level, which serves as a candidate of the CDW gap (inset of Fig. 3g) with a size similar to that detected in AV_3Sb_5 systems¹¹. Although there are weak in-plane superlattice modulations consistent with Fig. 2 from the topographic image, we clearly find the 2×2 charge modulation in the differential conductance map at E_F (Fig. 3h and its inset). The wavevectors from our electronic mapping (as marked by the red circles in the inset of Fig. 3h) match well with the in-plane vector of the CDW detected in Figs. 2 and 3a–d, supporting the electronic nature of the charge order (Extended Data Fig. 9a).

Having confirmed the presence of CDW, we now examine the potential origin of such CDW from the perspective of the electronic

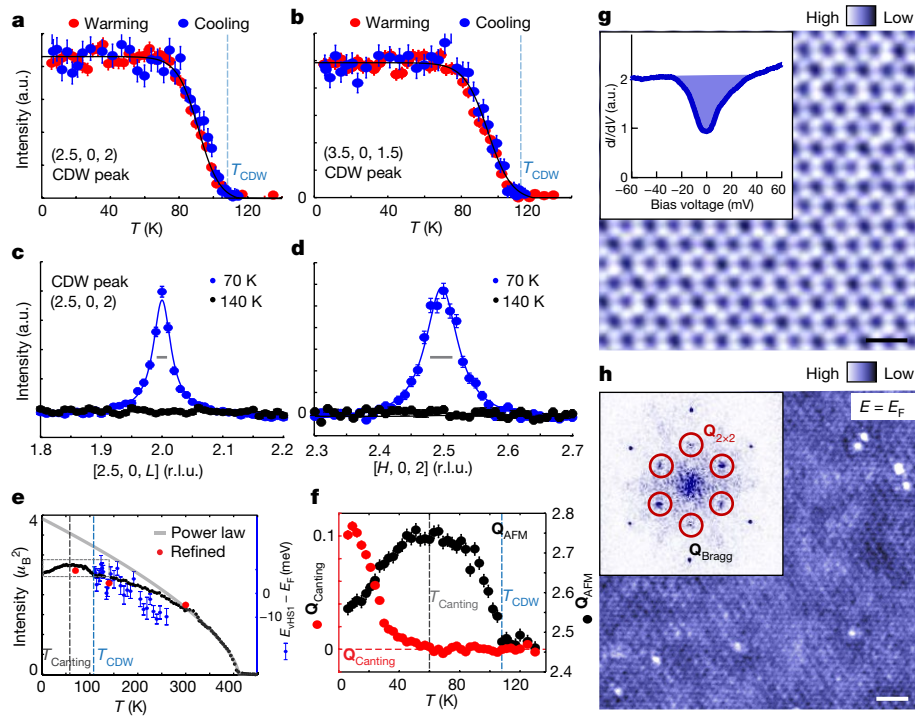


Fig. 3 | Order parameter of CDW and magnetic peaks, line shape of CDW peaks and STM results. **a, b**, Order parameter of CDW peaks at (2.5, 0, 2) and (3.5, 0, 1.5), respectively. Blue dots show data taken during cooling, whereas red dots show data taken during warming. **c, d**, Line shape of the CDW peak at (2.5, 0, 2) along the L and H directions, respectively. Integration range is ± 0.1 r.l.u. Blue lines are Lorentzian fits of the CDW peaks. Thick grey lines are FWHM of lattice peaks obtained by Gaussian fits. **e**, Order parameter of the magnetic peak at $\mathbf{Q}_{\text{AFM}} = (2, 0, 0.5)$. The grey line is a power law fit using $I = 3.86 \left(1 - \frac{T}{T_N}\right)^{\beta}$ with $T_N = 410.3$ K and $\beta = 0.325$. Red dots are refined magnetic moment size. Blue dots are energy location of vHS1 as determined from ARPES (T.X., manuscript in preparation). A sudden increase in magnetic moment is observed at T_{CDW} . **f**, Low-temperature magnetic order parameter. Black and red dots are

commensurate and incommensurate magnetic order parameters, respectively. At T_{Canting} , magnetic Bragg peaks at $\mathbf{Q} = (2, 0, 0.5 \pm \delta)$ emerge when the intensity of commensurate magnetic peak starts to decrease. The vertical error bars in **a–f** are statistical errors of 1 standard deviation. **g**, Atomically resolved topographic image of FeGe with bias voltage $V = 60$ mV and tunnelling current $I = 0.5$ nA. The inset shows the differential conductance data, showing a partially opened energy gap. The tunnelling spectrum is taken with $V = 60$ mV, $I = 0.5$ nA and a bias modulation of 0.5 mV. Scale bar, 1 nm. **h**, Differential conductance map taken at the Fermi level and its Fourier transform (inset). The red circles mark the in-plane 2×2 charge order vector. The map is taken with $V = 60$ mV, $I = 0.5$ nA and a bias modulation of 5 mV. Scale bar, 3 nm. All the STM data are taken at 4.2 K.

structure, as measured by ARPES at 140 K above T_{CDW} . From a detailed photon energy dependence measurement, we have identified 69-eV and 47-eV photons to investigate the Γ ($k_z = 0$) and A ($k_z = \pi$) points of the non-magnetic structural BZ, respectively (Extended Data Fig. 9b). The Fermi surfaces investigated across both k_z extrema are reminiscent of other kagome metals^{4,33,34}, consisting of rounded triangular pockets enclosing small pockets at the K points of the BZ (Fig. 4a). In particular, we identify quasi-straight sections of the Fermi surface connected at the M and L points, similar to those found in AV_3Sb_5 (refs. ^{33,34}). Notably, we identify two vHSs in proximity of the Fermi level at the M point and one at the L point of the BZ. This can be seen by tracing the dispersions across the M and L points, respectively. Along the direction parallel to the M - K direction, two dispersions are hole-like, in which their band top extrapolated from the observable portions of the dispersions traces out electron bands in the orthogonal direction along Γ - M , indicating their saddle-point nature (vHS1 and vHS2 in Fig. 4c). We note that vHS1 is located about 10 meV above the Fermi level, whereas vHS2 is about 50 meV below E_F . At the L point, we also identify vHS3, which is similar to vHS1 of the M point, located approximately 10 meV above E_F (Fig. 4d). Because these features are identified in the state immediately above the onset of the CDW, one can consider a nesting scenario in which vHS2 at M below E_F nests with vHS3 at L above E_F , giving rise to a $\mathbf{Q}_{\text{CDW}1}$ of (0.5, 0, 0.5)/(0, 0.5, 0.5), whereas vHS2 at M below E_F nests with vHS1 at neighbouring M s above E_F to give rise to a $\mathbf{Q}_{\text{CDW}2}$ of (0.5, 0, 0)/(0, 0.5, 0). The observation of these vHSs and quasi-straight sections of the Fermi

surface separated by the \mathbf{Q} s seen by neutron diffraction would be compatible with a vHS-nesting-driven scenario for the charge order in the AV_3Sb_5 materials¹⁵.

Discussion

It is well established that kagome lattice hosts destructive interference-induced flat bands and vHSs^{4,5}. For FeGe, the kagome-derived flat bands at E_F in the paramagnetic state could drive the system into antiferromagnetically coupled FM planes below T_N (ref. ³⁸). In each FM layer, magnetic order breaks the degeneracy of the electronic bands, splitting the spin-majority and spin-minority electronic bands that shift with temperature such that the nesting of vHSs in Fig. 4a to form CDW becomes possible. This has indeed led to a shift of the vHSs from higher binding energies towards E_F as the magnetic moment orders with temperature decreasing towards T_{CDW} (T.X., manuscript in preparation) (Fig. 3e).

As we observe AHE below the CDW similar to AV_3Sb_5 (refs. ^{24–28}), we speculate that the CDW in FeGe may also be associated with a chiral flux phase of circulating currents (Fig. 1l). At zero field, the chiral circulating currents in each FM kagome plane appearing below T_{CDW} produce c -axis aligned and anti-aligned magnetic fields that enhance the iron-ordered moment (left panels of Fig. 1l). Because the circulating currents have opposite directions in two adjacent iron kagome layers, there would be no net magnetization arising from the circulating currents and, therefore, no observable AHE. When a c -axis field is applied, one would

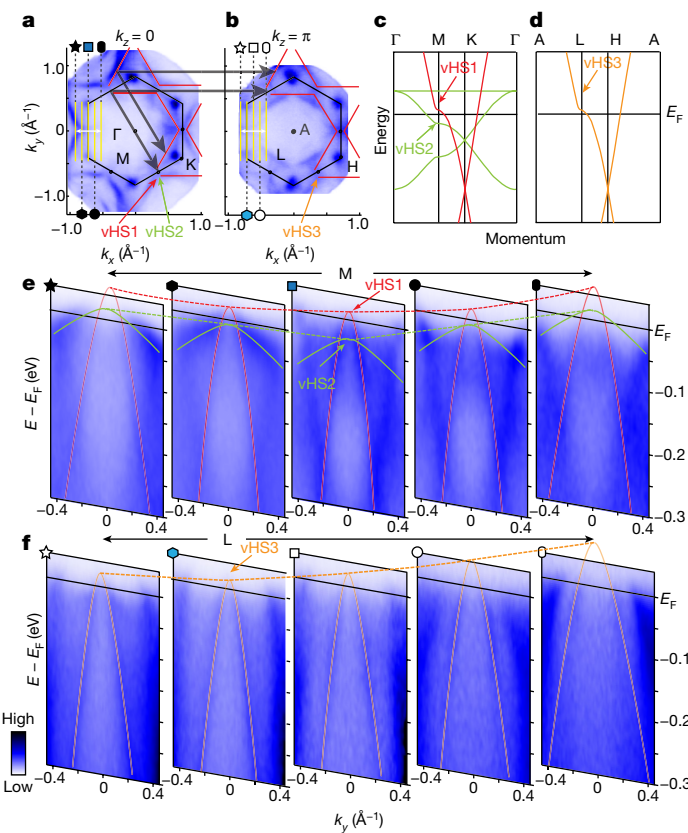


Fig. 4 | Schematic and ARPES data of vHSSs in AFM FeGe. **a,b**, ARPES-measured Fermi surfaces across $k_z = 0$ and $k_z = \pi$ using 69-eV and 47-eV photons, respectively. Polarization used was linear horizontal. Red lines indicate quasi-straight sections of the Fermi surface connected by \mathbf{Q}_{CDW} (grey arrows). Yellow lines mark out each cut in **e** and **f**. **c,d**, Schematic of the vHSSs in the FeGe electronic structure. **e,f**, Dispersions across the vHSSs. Solid and dashed lines mark out dispersion of vHSSs along the k_y and k_x directions, respectively. Cuts in **e**

are taken at $k_x = -0.93, -0.83, -0.73, -0.63$ and -0.53 \AA^{-1} in the $k_z = 0$ plane. Blue square indicates the K-M-K cut. Cuts in **f** are taken at $k_x = -0.79, -0.73, -0.63, -0.53$ and -0.43 \AA^{-1} in the $k_z = \pi$ plane. Blue hexagon indicates the H-L-H cut. The vHSSs are electron-like along the Γ -M- Γ (A-L-A) direction and hole-like along the K-M-K (H-L-H) direction. There are two vHSSs at the M point: vHS1 is above the Fermi level, whereas vHS2 is below the Fermi level. Another vHS, vHS3, is located above the Fermi level at the L point. Data are all taken above T_{CDW} at 140 K.

expect two effects: (1) a spin-flop transition in which the iron moment direction changes from along the *c*-axis to mostly the in-plane direction (Fig. 1*i* and right panels of Fig. 1*l*) and (2) modulation of the circulating currents in favour of the field direction that would produce a net magnetization. When the Zeeman energy of an applied field is smaller than the spin anisotropy energy that aligns the *c*-axis moment, there would be no spin-flop transition and the system is essentially the same as the zero-field state with no AHE.

When the Zeeman energy of a *c*-axis field overcomes the spin anisotropy energy, a spin-flop transition occurs, in which most of the moments are aligned parallel to the FeGe plane. In principle, the net magnetization induced by the canted iron moments along the *c*-axis can contribute to AHE, but the near-zero AHE above T_{CDW} (Fig. 1*k* and right panels of Fig. 1*l*) suggests that the contribution from canted moments along the *c*-axis is negligible. In the CDW state, the applied *c*-axis field will enhance the circulating currents in the kagome layers with aligned fields and suppress the circulating currents in the layers with anti-aligned fields, therefore producing a net FM moment to induce the observed AHE. As the field-induced spin-flop phase should be maintained below T_{Canting} (right panels of Fig. 1*l*), we do not expect the zero-field canted AFM phase to affect AHE (Fig. 1*k*). Although we have used chiral flux phase of circulating currents to explain our data, it is clear that electron correlations independent from Fermi surface nesting of vHSSs may also explain CDW order and its coupling with magnetism³⁹. Regardless of the theoretical explanation, we have identified a kagome metal system in FeGe in which strong electron correlations lead to a rich interplay of magnetic order, topology, CDW

and AHE. The CDW that we have found uniquely emerges within and strongly couples to a well-formed magnetic order, distinct from that of the stripe phase in cuprates^{1,2} and nickelates^{29–31}, and offers a new platform for exploring emergent phenomena in strongly correlated topological materials.

Online content

Any methods, additional references, Nature Research reporting summaries, source data, extended data, supplementary information, acknowledgements, peer review information; details of author contributions and competing interests; and statements of data and code availability are available at <https://doi.org/10.1038/s41586-022-05034-z>.

1. Kivelson, S. A. et al. How to detect fluctuating stripes in the high-temperature superconductors. *Rev. Mod. Phys.* **75**, 1201–1241 (2003).
2. Tranquada, J. M. Cuprate superconductors as viewed through a striped lens. *Adv. Phys.* **69**, 437–509 (2020).
3. Yin, J.-X. et al. Giant and anisotropic many-body spin-orbit tunability in a strongly correlated kagome magnet. *Nature* **562**, 91–95 (2018).
4. Kang, M. et al. Dirac fermions and flat bands in the ideal kagome metal FeSn. *Nat. Mater.* **19**, 163–169 (2020).
5. Mazin, I. I. et al. Theoretical prediction of a strongly correlated Dirac metal. *Nat. Commun.* **5**, 4261 (2014).
6. Ye, L. et al. Massive Dirac fermions in a ferromagnetic kagome metal. *Nature* **555**, 638–642 (2018).
7. Yin, J.-X. et al. Quantum-limit Chern topological magnetism in TbMn₆Sn₆. *Nature* **583**, 533–536 (2020).
8. Wang, Q. et al. Field-induced topological Hall effect and double-fan spin structure with a *c*-axis component in the metallic kagome antiferromagnetic compound YMn₆Sn₆. *Phys. Rev. B* **103**, 014416 (2021).

9. Ghimire, N. J. et al. Competing magnetic phases and fluctuation-driven scalar spin chirality in the kagome metal YMn_6Sn_8 . *Sci. Adv.* **6**, eabe2680 (2020).
10. Ortiz, B. R. et al. CsV_3Sb_5 : a Z_2 topological kagome metal with a superconducting ground state. *Phys. Rev. Lett.* **125**, 247002 (2020).
11. Jiang, Y.-X. et al. Unconventional chiral charge order in kagome superconductor KV_3Sb_5 . *Nat. Mater.* **20**, 1353–1357 (2021).
12. Liang, Z. et al. Three-dimensional charge density wave and surface-dependent vortex-core states in a kagome superconductor CsV_3Sb_5 . *Phys. Rev.* **11**, 031026 (2021).
13. Zhao, H. et al. Cascade of correlated electron states in the kagome superconductor CsV_3Sb_5 . *Nature* **599**, 216–221 (2021).
14. Chen, H. et al. Roton pair density wave in a strong-coupling kagome superconductor. *Nature* **599**, 222–228 (2021).
15. Neupert, T., Denner, M. M., Yin, J.-X., Thomale, R. & Hasan, M. Charge order and superconductivity in kagome materials. *Nat. Phys.* **18**, 137–143 (2022).
16. Ohoyama, T., Kanematsu, K. & Yasukōchi, K. A new intermetallic compound FeGe . *J. Phys. Soc. Jpn.* **18**, 589–589 (1963).
17. Beckman, O., Carrander, K., Lundgren, L. & Richardson, M. Susceptibility measurements and magnetic ordering of hexagonal FeGe . *Phys. Scr.* **6**, 151–157 (1972).
18. Bernhard, J., Lebech, B. & Beckman, O. Neutron diffraction studies of the low-temperature magnetic structure of hexagonal FeGe . *J. Phys. F: Met. Phys.* **14**, 2379–2393 (1984).
19. Bernhard, J., Lebech, B. & Beckman, O. Magnetic phase diagram of hexagonal FeGe determined by neutron diffraction. *J. Phys. F: Met. Phys.* **18**, 539–552 (1988).
20. Sales, B. C. et al. Electronic, magnetic, and thermodynamic properties of the kagome layer compound FeSn . *Phys. Rev. Mater.* **3**, 114203 (2019).
21. Xie, Y. et al. Spin excitations in metallic kagome lattice FeSn and CoSn . *Commun. Phys.* **4**, 240 (2021).
22. Yang, S.-Y. et al. Giant, unconventional anomalous Hall effect in the metallic frustrated magnet candidate, KV_3Sb_5 . *Sci. Adv.* **6**, eabb6003 (2020).
23. Yu, F. H. et al. Concurrence of anomalous Hall effect and charge density wave in a superconducting topological kagome metal. *Phys. Rev. B* **104**, L041103 (2021).
24. Haldane, F. D. M. Model for a quantum Hall effect without Landau levels: condensed-matter realization of the “parity anomaly”. *Phys. Rev. Lett.* **61**, 2015–2018 (1988).
25. Varma, C. M. Non-Fermi-liquid states and pairing instability of a general model of copper oxide metals. *Phys. Rev. B* **55**, 14554–14580 (1997).
26. Denner, M. M., Thomale, R. & Neupert, T. Analysis of charge order in the kagome metal AV_3Sb_5 ($A = \text{K}, \text{Rb}, \text{Cs}$). *Phys. Rev. Lett.* **127**, 217601 (2021).
27. Mielke, C. et al. Time-reversal symmetry-breaking charge order in a correlated kagome superconductor. *Nature* **602**, 245–250 (2022).
28. Feng, X., Jiang, K., Wang, Z. & Hu, J. Chiral flux phase in the kagome superconductor AV_3Sb_5 . *Sci. Bull.* **66**, 1384–1388 (2021).
29. Tranquada, J. M., Butrey, D. J., Sachan, V. & Lorenzo, J. E. Simultaneous ordering of holes and spins in $\text{La}_2\text{NiO}_{4.125}$. *Phys. Rev. Lett.* **73**, 1003–1006 (1994).
30. Lee, S. H. & Cheong, S. W. Melting of quasi-two-dimensional charge stripes in $\text{La}_{1.5}\text{Sr}_{1/2}\text{NiO}_3$. *Phys. Rev. Lett.* **79**, 2514–2517 (1997).
31. Zhang, J. et al. Intertwined density waves in a metallic nickelate. *Nat. Commun.* **11**, 6003 (2020).
32. Grüner, G. The dynamics of charge-density waves. *Rev. Mod. Phys.* **60**, 1129–1181 (1988).
33. Liu, Z. et al. Charge-density-wave-induced bands renormalization and energy gaps in a kagome superconductor RbV_3Sb_5 . *Phys. Rev.* **11**, 041010 (2021).
34. Kang, M. et al. Twofold van Hove singularity and origin of charge order in topological kagome superconductor CsV_3Sb_5 . *Nat. Phys.* **18**, 301–308 (2022).
35. Si, Q. & Abrahams, E. Strong correlations and magnetic frustration in the high T_c iron pnictides. *Phys. Rev. Lett.* **101**, 076401 (2008).
36. Nagaosa, N., Sinova, J., Onoda, S., MacDonald, A. H. & Ong, N. P. Anomalous Hall effect. *Rev. Mod. Phys.* **82**, 1539–1592 (2010).
37. Suzuki, T. et al. Large anomalous Hall effect in a half-Heusler antiferromagnet. *Nat. Phys.* **12**, 1119–1123 (2016).
38. Huang, L. & Lu, H. Signatures of Hundness in kagome metals. *Phys. Rev. B* **102**, 125130 (2020).
39. Setty, C., Hu, H., Che, L. & Si, Q. Electron correlations and T -breaking density wave order in a Z_2 kagome metal. Preprint at <https://arxiv.org/abs/2105.15204> (2021).
40. Richardson, M. The partial equilibrium diagram of the $\text{Fe}-\text{Ge}$ system in the range 40–72 at.% Ge, and the crystallisation of some iron germanides by chemical transport reactions. *Acta Chem. Scand.* **21**, 2305–2317 (1967).

Publisher's note Springer Nature remains neutral with regard to jurisdictional claims in published maps and institutional affiliations.

Springer Nature or its licensor holds exclusive rights to this article under a publishing agreement with the author(s) or other rightsholder(s); author self-archiving of the accepted manuscript version of this article is solely governed by the terms of such publishing agreement and applicable law.

© The Author(s), under exclusive licence to Springer Nature Limited 2022, corrected publication 2022

Methods

Sample synthesis, structural and composition characterizations
 Polycrystalline FeGe samples were grown by a solid-state method⁴⁰. Stoichiometric Fe (99.95%, Alfa Aesar) and Ge (99.999%, Alfa Aesar) powders were mixed, ground and pressed into a pellet inside an argon glovebox. The pellet was loaded inside an Al_2O_3 crucible and sealed in an evacuated quartz tube. It was sintered in a box furnace at 1,000 °C for 7 days, then at 700 °C for 7 days. Single-crystalline FeGe was grown by the chemical vapour transport method⁴⁰. The pellet was ground to powder and then loaded into a sealed quartz tube together with iodine lumps as the transport agent. The temperatures at feedstock and crystallization regions were set to 570 °C and 545 °C, respectively, for 3 weeks. Millimetre-sized FeGe single crystals were found at the cold end (inset of Extended Data Fig. 1e). Extended Data Fig. 1a shows the X-ray Laue pattern of the crystal and Extended Data Fig. 1b plots refinement results comparing calculated and observed Bragg peak intensity. We find no evidence of any other crystal structures, such as Fe_6Ge_5 and Fe_2Ge_3 , as impurity phases⁴¹ because the X-ray and neutron diffraction patterns of these structures^{42,43} are different from the diffraction patterns shown in Fig. 2d and Extended Data Fig. 1a.

To further confirm that the 100-K feature in Fig. 1f is indeed associated with superlattice distortion, we carried X-ray Laue diffraction experiments at 150 K and 50 K. Extended Data Fig. 1c,d shows the diffraction pattern in the $[H, K, 0.5]$ zone at 150 K and 50 K, respectively. Although there are no observable superlattice peaks at 150 K, superlattice peaks at half-integer points appear at 50 K, consistent with neutron scattering data of Fig. 2. Because conventional X-ray scattering will not be sensitive to magnetic order, these results further confirm the lattice distortion nature of the superlattice peaks associated with CDW order.

To determine the sample stoichiometry, we carried out elemental analysis using energy-dispersive X-ray (EDX) spectroscopy analysis in a FEI Nano 450 scanning electron microscope on three batches of polished FeGe single crystals. The average stoichiometry of each crystal was determined by examination of several points and the outcome suggests that the atomic ratio of Fe:Ge is close to 1:1 (Extended Data Fig. 1e).

To confirm the crystalline quality and stoichiometry of the samples used in our experiments, we perform X-ray single-crystal diffraction experiment at the Rigaku XtaLAB PRO diffractometer housed at the Spallation Neutron Source at Oak Ridge National Laboratory. The measured crystals were suspended in Paratone oil and mounted on a plastic loop attached to a copper pin/goniometer. The single-crystal X-ray diffraction data were collected with molybdenum $\text{K}\alpha$ radiation ($\lambda = 0.71073 \text{ \AA}$) at 150 K. More than 4,500 diffraction Bragg peaks were collected and refined using Rietveld analysis. The refinement results indicate that the Ge2 and Fe sites are fully occupied and the occupancy at the Ge1 site is 95%. The results indicate that the single crystals are essentially fully stoichiometric with chemical formula $\text{Fe}_{1.00}\text{Ge}_{0.98}$.

Magnetic susceptibility and heat capacity measurements

Extended Data Fig. 2 summarizes the magnetic field dependence of susceptibility measured using a Quantum Design physical property measurement system (PPMS) at Rice. For the in-plane applied field, we see increasing susceptibility with increasing field that is weakly temperature-dependent across T_{CDW} , consistent with canting of the moment along the field direction (Extended Data Fig. 2a). When the field is applied along the c -axis, spin-flop shown in the inset of Fig. 1e occurs above a critical field, in which magnetization increases suddenly owing to spin canting. The critical field for spin-flop transition decreases slightly in the CDW phase, as clearly seen in Extended Data Fig. 2b,c. These results are consistent with earlier work¹⁷ and our inelastic neutron scattering experiments that show a decrease in spin anisotropy gap with decreasing temperature below T_{Canting} . Extended Data Fig. 2d shows the temperature dependence of the heat capacity, which confirms that CDW transition is a bulk phase transition.

Transport measurements

Electrical and magneto-transport measurements were carried out in a 14-T PPMS. Samples were made in a standard four-probe or six-probe contact configuration with current direction in-plane and magnetic field out of the plane (c -axis). To eliminate any effects from contact misalignment, the Hall resistivities were symmetrized and anti-symmetrized, respectively. Extended Data Fig. 3a,b shows the magnetic field dependence of Hall resistivity at temperatures across T_{CDW} . There is a clear jump in the Hall resistivity across the spin-flop transition at temperatures above and below T_{CDW} , but the magnitude of the jump becomes smaller with decreasing temperature and changes sign for temperatures approximately below T_{Canting} .

The field dependence of Hall resistivity in the A-type AFM state is described by $\rho_{xy} = R_1 H$ for $H < H_c$, in which R_1 is the ordinary Hall coefficient in the AFM state determined by the electronic structure and the scattering rates in the AFM state, H is the magnitude of the applied field, and H_c is the critical field needed to induce a spin-flop transition. In the field-induced spin-flop state $H > H_c$, we have $\rho_{xy} = R_2 H + \rho_{\text{AHE}}$, in which R_2 is the ordinary Hall coefficient in the spin-flop state determined by the electronic structure and the scattering rates in spin-flop state and ρ_{AHE} is the anomalous Hall resistivity resulting from the finite magnetization induced by the spin-flop. Therefore, the jump of Hall resistivity at the spin-flop transition in Extended Data Fig. 3a,b is determined by both the change of ordinary Hall coefficient and the anomalous Hall resistivity.

Extended Data Fig. 3c,f shows temperature-dependent Hall carrier density and Hall mobility calculated from the Hall coefficient and zero-field resistivity by assuming a single-band model. Notice that FeGe is a multiband system. The carrier density and mobility shown here are only effective parameters determined by the carrier density and mobility of each band. Nevertheless, we see a clear reduction in electron density across T_{CDW} . Temperature and field dependence of ρ_{xy} and $d\rho_{xy}/dH$ are shown in Extended Data Fig. 3d,e, respectively. Extended Data Fig. 3g,h shows field hysteresis of ρ_{xy} below and above T_{CDW} , respectively.

Neutron scattering experiments

Neutron scattering measurements on FeGe were carried out on the CORELLI⁴⁴ spectrometer of the Spallation Neutron Source at Oak Ridge National Laboratory. A single crystal of about 30 mg is mounted inside a closed-cycle refrigerator with a base temperature of 6 K and the Mantid package was used for data reduction and analysis. We define the momentum transfer \mathbf{Q} in 3D reciprocal space in \AA^{-1} as $\mathbf{Q} = H\mathbf{a}^* + K\mathbf{b}^* + L\mathbf{c}^*$, in which H, K and L are Miller indices and $\mathbf{a}^* = 2\pi(\mathbf{b} \times \mathbf{c})/[\mathbf{a} \cdot (\mathbf{b} \times \mathbf{c})]$, $\mathbf{b}^* = 2\pi(\mathbf{c} \times \mathbf{a})/[\mathbf{a} \cdot (\mathbf{b} \times \mathbf{c})]$ and $\mathbf{c}^* = 2\pi(\mathbf{a} \times \mathbf{b})/[\mathbf{a} \cdot (\mathbf{b} \times \mathbf{c})]$, with $\mathbf{a} = a\hat{\mathbf{x}}$, $\mathbf{b} = a(\cos 120^\circ \hat{\mathbf{x}} + \sin 120^\circ \hat{\mathbf{y}})$ and $\mathbf{c} = c\hat{\mathbf{z}}$ (Fig. 2a,b). Extended Data Fig. 4 shows the raw neutron scattering data in the horizontal $[H, 0, L]$ scattering plane, where broad CDW peaks are seen at $\mathbf{Q}_{\text{CDW1}} = (0.5, 0, 0.5)$ and $\mathbf{Q}_{\text{CDW2}} = (0.5, 0, 0)$. To determine the instrumental resolution and compare with the width of CDW peaks, we show in Extended Data Fig. 4 scans along different directions for nuclear Bragg peaks (Fig. 4a-d), AFM Bragg peaks (Fig. 4e,f) and CDW peaks (Fig. 4g-l). We find that CDW peaks are best fit by Lorentzian line shape, contrasting to typical Gaussian fits for nuclear and magnetic Bragg peaks.

Estimation of canting angle. In the spin-flop phase, the Zeeman energy generated by a c -axis magnetic field is enough to overcome the magnetic anisotropy, yet not enough to overcome exchange interactions between interlayer AFM Fe atoms, hence the net effect will be that the spins turn 90° into the ab plane and have a small canting towards the magnetic field direction. Here, by estimating the order of magnitude of the exchange interaction, we estimate the canting angle after the spin-flop transition under a 10-T field.

Assuming Fe has classical spin $S=1, g=2$, the Zeeman energy generated by a $B=10$ T field is $E_z = \mu_B S B = 1.15 \text{ meV}$, which is comparable

with the magnetic anisotropy. The AFM T_N of FeGe is around 410 K, corresponding to the inter-planar exchange $J_c = k_B T_N / (gS)$ of approximately 17 meV, consistent with spin-wave measurements. The characteristic canting angle is determined by the ratio between anisotropy and exchange interactions:

$$\theta = \frac{g\mu_B SB}{ZJ_c}$$

Using $B = 10$ T, J_c of around 17 meV and neighbouring atom number $Z = 2$, we get θ of about 1.9°.

The canting angle of about 2° can be further confirmed by the magnetic moment induced by a 10-T field. The magnetic moment under a 10-T c-axis field at 70 K is about 4 emu g⁻¹ = (4.3 × 10²⁰ μ_B)/(4.69 × 10²¹) atoms. Therefore, every Fe atom will have around 0.09 μ_B moment, which indicates $gS_z = 0.09$, and the canting angle calculated here is $\arcsin(0.09/2) = 2.6^\circ$, consistent with the estimation from exchange couplings.

Magnetic form factor of the circulating currents. The magnetic form factor is the Fourier transform of the magnetic moment in the reciprocal space. In FeGe, there are two types of moment in the CDW flux phase: the moment directly from the magnetic flux induced by circulating charge current (Fig. 1d) or the moment from the Fe ion. The magnetic form factor of the former is determined by the size of the hexagon/triangle in the kagome lattice, whereas the latter has the form factor of the Fe atom itself. Extended Data Fig. 5a–f shows the in-plane magnetic form factor generated by the Fourier transform of hexagonal and triangular flux units. Both units have the edge length of $a/2$. Compared with the Fe magnetic form factor, the hexagon form factor decays much faster with increasing $|Q|$, whereas the triangle form factor is comparable with that of Fe. Furthermore, one would expect the Fe magnetic form factor to be isotropic in reciprocal space, with the form factor from circulating currents to be highly anisotropic in reciprocal space, as the current is confined within the kagome layer.

Extended Data Fig. 5g shows the Q dependence of the enhanced neutron intensity by subtracting 140 K magnetic peak intensity from 70 K including both in-plane and out-of-plane magnetic Bragg peaks. We compare it with the Q dependence of the Fe magnetic peaks at 140 K, which should only have Fe moment, and find that they are almost identical. Therefore, the enhanced moment must come from Fe atoms. Furthermore, the CDW peak structure factor increases with increasing Q , suggesting that it originates from lattice distortion or modulation (Extended Data Fig. 5h).

Non-magnetic peaks at ($H, 0, -4.5$) positions. Figure 2e,f shows neutron diffraction patterns at 140 K and 70 K, respectively, in the $[H, 0, L]$ plane. At 140 K, we find nuclear and magnetic Bragg peaks at $(H, 0, L)$ and $(H, 0, L+1/2)$ positions, respectively. At 70 K, we expect superlattice peaks resulting from CDW to appear at $(H+1/2, 0, L+1/2)$ positions and magnetic peaks at $(H, 0, L+1/2)$ to follow the Fe magnetic form factor and become vanishingly small at large wavevectors. However, there is a weak peak at $(7, 0, -4.5)$, which should have vanishingly small magnetic form factor owing to its large Q , at 70 K (Fig. 2f) that is not present at 140 K (Fig. 2e). To determine whether this peak has a non-magnetic origin, we calculate the expected magnetic structural factor of A-type antiferromagnet without considering the magnetic form factor and divide that into the observed integrated intensity at all expected magnetic positions $(H, 0, L+1/2)$. If the observed scattering has a magnetic origin, the outcome of the division should follow the Fe magnetic form factor. Extended Data Fig. 6a,b shows the systematic analysis in this way at 140 K and 70 K, respectively. At 140 K ($>T_{CDW}$), most Bragg peaks (including $(2, 0, 1/2)$) at the AFM wavevector agree with the Fe magnetic form factor (solid orange line), except with small deviations at the $(1, 0, 3.5)$ and $(1, 0, 1.5)$ positions at which aluminium powder ring

background overlaps with these peaks (Fig. 2). At 70 K ($<T_{CDW}$), whereas the majority of the AFM positions still conform with the Fe magnetic form factor, the scattering intensity at $(H, 0, -4.5)$ positions with $H = 2, 3, 5$ and 7 deviate from the expected behaviour and, therefore, have a non-magnetic origin. We carefully examined possible structural superlattice peaks at all other $(H, 0, L+1/2)$ positions, including $L = 0, 1, 2, 3$ and 5, but find no (weak) evidence for them. Although the origin of non-magnetic peaks at $(H, 0, -4.5)$ remains unclear, we can assume that they have a superlattice origin and estimate the impact on the observed intensity gain at $(2, 0, 1/2)$, which has the strongest magnetic scattering intensity from the A-type antiferromagnet, across the T_{CDW} transition. Extended Data Fig. 6c shows the integrated scattering intensity at all $(H, 0, L+1/2)$ and $(H+1/2, 0, L+1/2)$ positions at 70 K, together with the scattering intensity of $(2, 0, 1/2)$ at 140 K. Although the CDW scattering intensity at $(H+1/2, 0, L+1/2)$ positions increases with increasing Q , consistent with the properties of lattice-distortion-induced superlattice peaks, their absolute intensities near the $(2, 0, 1/2)$ position are still much lower than the observed intensity gain at $(2, 0, 1/2)$ (solid red circles near 3 Å⁻¹ and dashed yellow line). If the $(7, 0, -4.5)$ peak has a superlattice origin, we can scale its intensity to the $(2, 0, 1/2)$ position, assuming that the intensity is proportional to Q . This extrapolation gives a possible lattice intensity at $(2, 0, 1/2)$ of 0.083 (green bars in Extended Data Fig. 6c,d), which is approximately 1.8% of the AFM Bragg peak intensity. However, the intensity enhancement we observe at $(2, 0, 1/2)$ from 140 K to 70 K is about 12% (dashed yellow dashed in Extended Data Fig. 6c,d, with absolute value 0.5), which is six times larger than the presumed lattice component. Therefore, we conclude that the intensity enhancement at $(2, 0, 1/2)$ across $<T_{CDW}$ has a magnetic origin, although the non-magnetic peak at $(H, 0, -4.5)$ deserves further investigation.

CDW correlation lengths. In FeGe, the CDW phase has a smaller correlation length compared with that of magnetic order. As shown in Fig. 2, the Bragg peak for the magnetic ordering wavevectors is limited by resolution (that is, has the same full width at half maximum (FWHM) as lattice peaks), suggesting that the magnetic order is long range. On the other hand, the CDW Bragg peak has a larger FWHM when compared with magnetic or lattice peaks (Extended Data Fig. 4). In this section, we calculate the lower limit of the correlation length of CDW in FeGe using inverse Fourier transform of the CDW peaks. Here the words ‘lower limit’ mean we do not consider the peak broadening effect of the instrumental resolution.

The CDW peak is fit by a Lorentzian, $I_q = A \frac{1}{1 + (\frac{q-q_0}{y})^2}$, in which A is a constant, q_0 is the peak centre position and y is the half width at half maximum (=1/2 FWHM). Its Fourier transform will be $I_x = Ay \sqrt{\frac{\pi}{2}} e^{iq_0x} e^{-y|x|}$. The correlation length (CL) here is defined as the FWHM of $|I_x|$, therefore, $CL = 2\ln 2/y$. The fitting of the CDW peak gives $y_H = 0.0441$ Å⁻¹ and $y_L = 0.0273$ Å⁻¹ at $(2.5, 0, 2)$, and gives $y_H = 0.0395$ Å⁻¹ and $y_L = 0.0296$ Å⁻¹ at $(3.5, 0, 1.5)$. By averaging the width of the two peaks, we get the lower limit of $CL = 33.2$ Å along in-plane directions and $CL = 48.7$ Å along the c-axis.

Crystal and magnetic structure refinement results. To extract the absolute value of magnetic moment generated by Fe atoms, we performed crystal and magnetic structure refinement using the JANA2006 program⁴⁵ for CORELLI data at 300 K, 140 K and 70 K. Extended Data Fig. 7 shows temperature dependence of the scattering map within the $[H, K, 0.5]$ plane. The refinement results for magnetic structures are shown in Extended Data Fig. 8a–c. Note that the refinement is only performed on lattice and magnetic peaks at the CDW phase at 70 K, therefore the exclusion of the CDW peaks causes some missing intensity at the lattice Bragg peaks and, therefore, increases R_w under 70 K. However, the magnetic moment extracted at all three temperatures fits well with the temperature dependence of the order parameter as shown in Fig. 3e.

Article

These results confirm that magnetic structure is the *A*-type AFM at 300 K, 140 K and 70 K and does not change across CDW transition.

As for the incommensurate phase at 6 K, there are two propagation vectors, (0, 0, 1/2) and (0, 0, 0.46). JANA2006 program is not able to refine systems with several propagation vectors, thus we calculate the magnetic peak intensity using the formula^{18,19}:

$$F^2(\mathbf{q}) = A(f_{\text{Fe}}(\mathbf{q}))^2 |G_{HKL}|^2 \left[(1 - e_z^2) \delta(\mathbf{q} - \tau_{HKL}) \cos^2 \alpha + \frac{1}{4}(1 + e_z^2) \delta(\mathbf{q} + \mathbf{Q} - \tau_{HKL}) \delta(\mathbf{q} - \mathbf{Q} - \tau_{HKL}) \sin^2 \alpha \right]$$

in which A is a scaling constant, $f_{\text{Fe}}(\mathbf{q})$ is the magnetic form factor of Fe, $|G_{HKL}|$ is the geometrical structure factor for the (H, K, L) reflection for the Fe lattice, with $|G_{HKL}| = 6$ for even H and $|G_{HKL}| = 2$ for odd H in the $[H, 0, L]$ plane with half-integer or incommensurate L , e_z is the projection on the z -axis of the unit scattering vector $\mathbf{q}/|\mathbf{q}|$, τ_{HKL} is the reciprocal lattice vector for the (H, K, L) reflection ($(H, K, L) = (\text{integer}, \text{integer}, \text{half-integer})$), $\mathbf{Q} = (0, 0, 0.04)$ and α is the canting angle. Here only the canting angle is a non-trivial variable. Setting $\alpha = 18^\circ$, we calculate the Bragg reflections in the $[H, 0, L]$ plane as shown in Extended Data Figs. 8d,e. The calculated intensity matches well with the experimental data, confirming the correctness of the proposed magnetic structure in the incommensurate phase^{18,19}.

To understand superlattice peaks induced by the CDW order, we consider a simple model by introducing a small *c*-axis lattice distortion of Fe in an ideal structure of FeGe. The $2 \times 2 \times 2$ superstructure of the CDW phase can be used to simulate the half-integer lattice peak intensity observed at 70 K. Although the full refinement of the superstructure is a challenging task, we can still estimate the extent of lattice distortion induced by CDW using restricted refinements. Assuming that the lattice distortion is on Fe only, and is only along the out-of-plane direction, we can expect superlattice peaks with wavevectors at $(1/2, 1/2, 1/2)$ and equivalent positions. Under this assumption, we build a FeGe superlattice with $a^* = b^* = 2a = 9.98 \text{ \AA}$ and $c^* = 2c = 8.10 \text{ \AA}$, extracted all CDW and integer Bragg peaks from the 70-K data (excluding the magnetic peaks) and multiply the (H, K, L) coordinates by a factor of 2. If the CDW phase has the symmetry shown in Fig. 1d, the space group of the superlattice is then reduced to P622 (#177), and the two Fe coordinates are $(1/4, 0, 1/4 + \delta_{\text{cl}})$ for Fe1 and $(1/2, 1/4, 1/4 + \delta_{\text{cl}})$ for Fe2. Fixing all Ge atom positions, we used the JANA2006 program⁴⁵ to refine the two parameters δ_{cl} and δ_{c2} . The result, as shown in Extended Data Fig. 8f,g, gives $\delta_{\text{cl}} = 0.0067$ and $\delta_{\text{c2}} = 0.0022$, which correspond to 0.054 \AA and 0.018 \AA , respectively. This estimation implies that the Fe atom will have a distortion within approximately 1% of the original lattice parameter in the CDW phase (Extended Data Table 4).

STM measurements

Single crystals with size up to $2 \times 2 \times 0.3 \text{ mm}$ are cleaved mechanically in situ at 77 K in ultrahigh-vacuum conditions and then immediately inserted into the microscope head, already at ^4He base temperature (4.2 K). Topographic images in this work are taken with the tunnelling junction set-up $V = 60 \text{ mV}$ and $I = 0.05 \text{ nA}$. Tunnelling conductance spectra are obtained with an Ir/Pt tip using standard lock-in amplifier techniques with a lock-in frequency of 977 Hz and a junction set-up of $V = 60 \text{ mV}$ and $I = 1 \text{ nA}$ and a root-mean-square oscillation voltage of 0.5 mV . Tunnelling conductance maps are obtained with a junction set-up of $V = 60 \text{ mV}$ and $I = 0.3 \text{ nA}$ and a root-mean-square oscillation voltage of 5 mV . For correlated materials, it is not surprising that the CDW order is more often detected in dI/dV maps by STM.

Primary examples are cuprate superconductors (4a CDW order is mainly reported by dI/dV maps). We detected weak CDW order taken with bias voltages of -30 meV . We show in Extended Data Fig. 9a topographic data taken at -30 mV and their Fourier transform. Signatures of 2×2 charge order are marked by red circles in the Fourier transform data.

ARPES measurements

ARPES measurements were carried out at BL 5-2 of the Stanford Synchrotron Radiation Lightsource and the MAESTRO beamline (7.0.2) of the Advanced Light Source, with a DA30 electron analyser and a R4000 electron analyser with deflector mode, respectively. FeGe single crystals were cleaved in situ in ultrahigh vacuum with a base pressure better than $5 \times 10^{-11} \text{ torr}$. Energy and angular resolutions used were better than 20 meV and 0.1° , respectively. Extended Data Fig. 9b shows photon-energy-dependent ARPES measurements.

Data availability

The data that support the plots in this paper and other findings of this study are available from the corresponding authors on reasonable request.

41. Khalaniya, R. A. & Shevelkov, A. V. When two is enough: on the origin of diverse crystal structures and physical properties in the Fe-Ge system. *J. Solid State Chem.* **270**, 118–128 (2019).
42. Larsson, A.-K., Furuseth, S. & Withers, R. On the crystal structure of Fe_6Ge_5 and its relationship to B8-type structures. *J. Solid State Chem.* **141**, 199–204 (1998).
43. Wu, W.-Y. et al. Endotaxial growth of Fe_xGe single-crystals on Ge(001) substrates. *CrystEngComm* **20**, 2916–2922 (2018).
44. Ye, F., Liu, Y., Whitfield, R., Osborn, R. & Rosenkranz, S. Implementation of cross correlation for energy discrimination on the time-of-flight spectrometer CORELLI. *J. Appl. Crystallogr.* **51**, 315–322 (2018).
45. Petříček, V., Dušek, M. & Palatinus, L. Crystallographic computing system JANA2006: general features. *Z. Kristallogr. Cryst. Mater.* **229**, 345–352 (2014).

Acknowledgements We thank D. Xiao, Q. Si and C. Setty for helpful discussions. The neutron scattering and single-crystal synthesis work at Rice was supported by US NSF-DMR-2100741 and by the Robert A. Welch Foundation under grant no. C-1839, respectively. The ARPES work at Rice was supported by the U.S. Department of Energy (DOE) grant no. DE-SC0021421, the Gordon and Betty Moore Foundation's EPiQS Initiative through grant no. GBMF9470 and the Robert A. Welch Foundation grant no. C-2024. The transport experiment at the University of Washington was supported by the Air Force Office of Scientific Research under grant FA9550-21-1-0068 and the David and Lucile Packard Foundation. Experimental and theoretical work at Princeton University was supported by the Gordon and Betty Moore Foundation (GBMF4547 and GBMF9461; M.Z.H.) and the U.S. DOE under the Basic Energy Sciences programme (grant no. DOE/BES DE-FG-02-05ER46200). The work at the University of California, Berkeley was supported by the U.S. DOE under contract no. DE-AC02-05-CH11231 in the Quantum Materials Program (KC2202). This research used resources of the Advanced Light Source and the Stanford Synchrotron Radiation Lightsource, both U.S. DOE Office of Science User Facilities under contract nos. DE-AC02-05CH11231 and AC02-76SF00515, respectively. A portion of this research used resources at the Spallation Neutron Source, a DOE Office of Science User Facility operated by Oak Ridge National Laboratory.

Author contributions P.D. and M.Y. conceived and managed the project. The single-crystal FeGe samples were grown by X.T. and B.G. Neutron scattering and X-ray diffraction experiments were carried out by F.Y. in remote discussion with P.D. and X.T. Neutron refinements were carried out by X.T., L.C., and K.J.N. Magnetic susceptibility and heat capacity measurements were performed by X.T. and Y.X. Transport measurements were carried out by E.Rosenberg, Z.L. and J.-H.C. STM measurements were carried out by J.-X.Y., Y.-X.J. and M.Z.H. ARPES experiments were carried out by X.T., J.S.O., R.J.B. and M.Y., with the assistance of M.H., D.L., C.J., A.B. and E.Rotenberg. The paper is written by P.D., M.Y., J.-H.C., J.-X.Y., X.T. and L.C., and all co-authors made comments on the paper.

Competing interests The authors declare no competing interests.

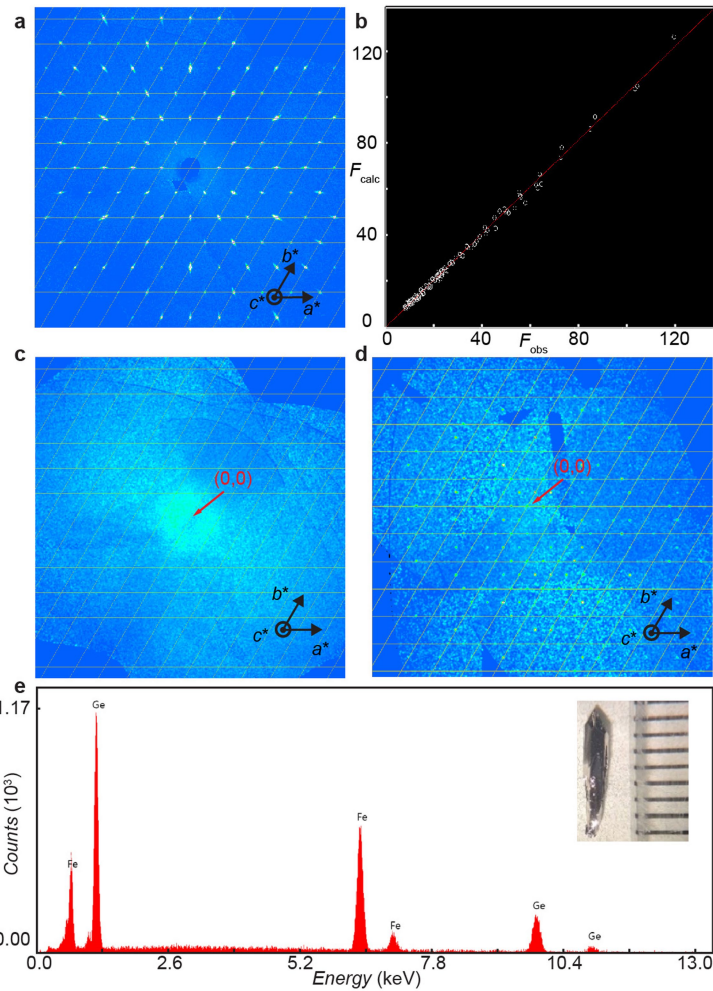
Additional information

Supplementary information The online version contains supplementary material available at <https://doi.org/10.1038/s41586-022-05034-z>.

Correspondence and requests for materials should be addressed to Ming Yi or Pengcheng Dai.

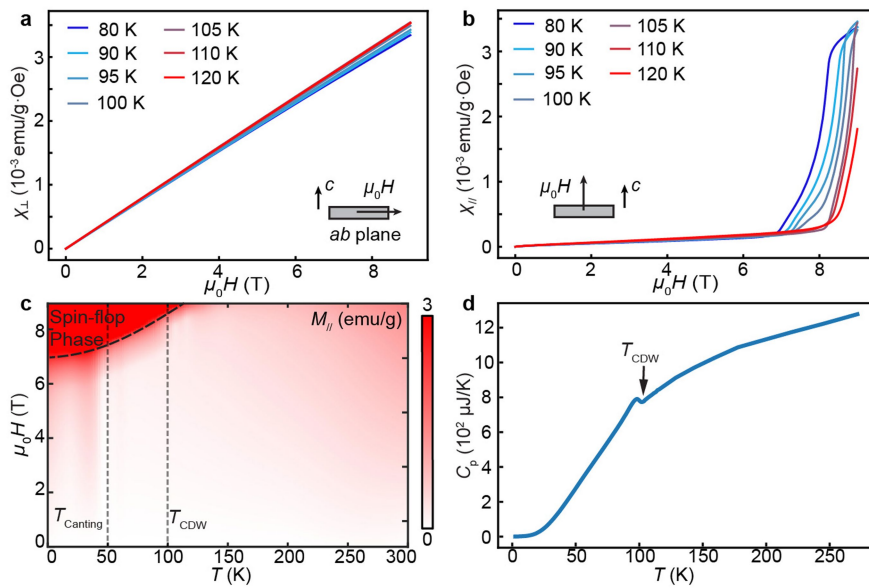
Peer review information *Nature* thanks Yuan Li and the other, anonymous, reviewer(s) for their contribution to the peer review of this work. Peer reviewer reports are available.

Reprints and permissions information is available at <http://www.nature.com/reprints>.



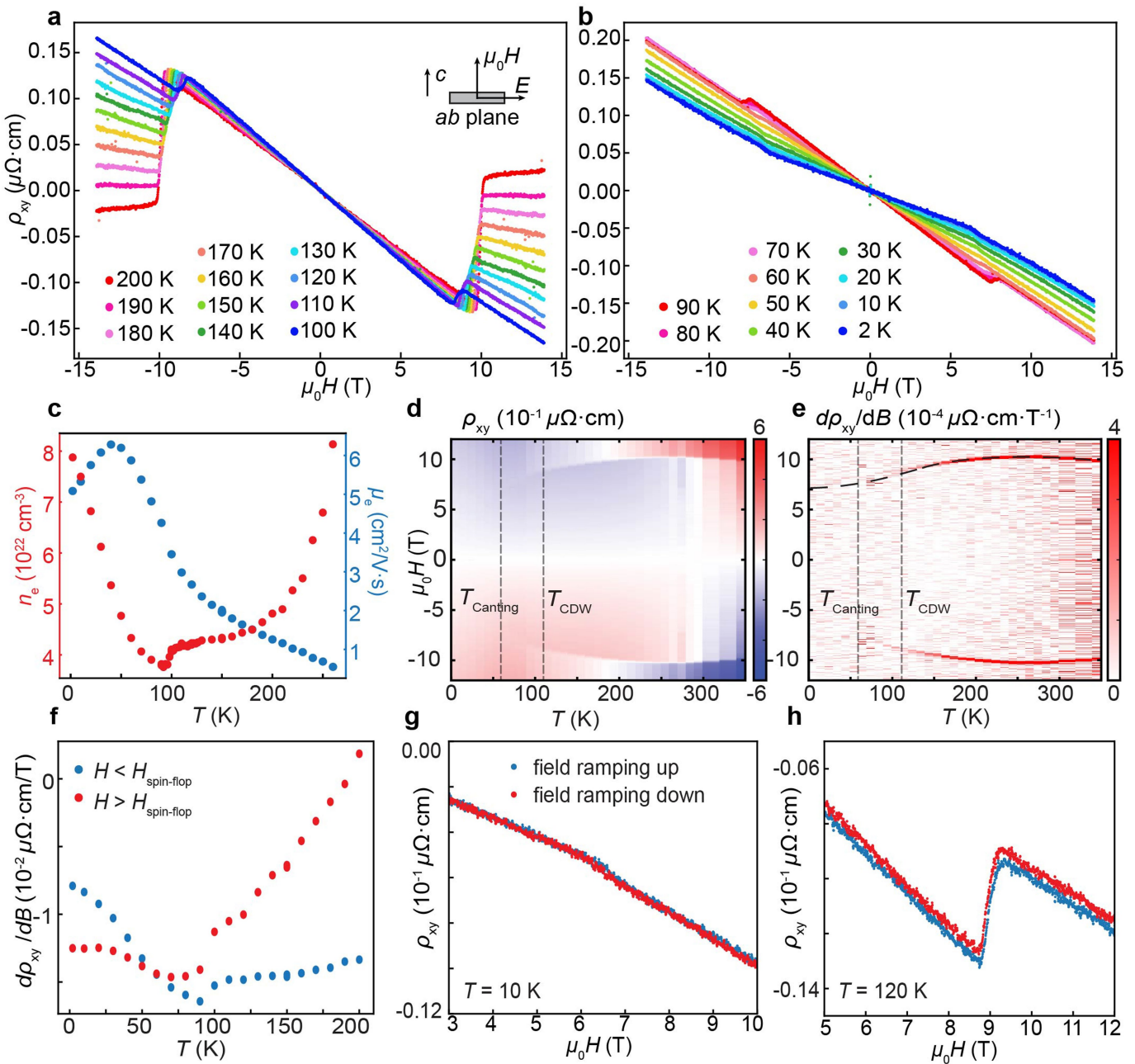
Extended Data Fig. 1 | X-ray pattern, structure refinement, EDX spectroscopy analysis and sample pictures of FeGe. **a**, X-ray diffraction pattern of the (0, 0, 1) plane. The strongest intensity is around 1,000 and the minimum is zero. **b**, Calculated structure factor F_{calc} versus observed structure factor F_{obs} from X-ray diffraction. The X-ray experiment is performed at 150 K. **c,d**, X-ray diffraction patterns of the (0, 0, 0.5) plane at 150 K and 50 K.

The strongest intensity at $L = 0.5$ is around 10 and the minimum is zero. **e**, EDX spectroscopy analysis in a FEI Nano 450 scanning electron microscope, which shows that the atomic ratios of Fe and Ge are $52 \pm 3\%$ and $48 \pm 5\%$, respectively. Measurement is performed at room temperature using a voltage of 20 kV. Counting time is 30 s. Inset of **e** shows a piece of FeGe single crystal. Tick size is 1 mm.



Extended Data Fig. 2 | Magnetic susceptibility, phase diagram and heat capacity of FeGe single crystal. **a,b**, Magnetic susceptibility with field perpendicular to the c -axis χ_{\perp} (**a**) and parallel to the c -axis χ_{\parallel} (**b**) versus magnetic field at various temperatures. Spin-flop field keeps decreasing with decreasing

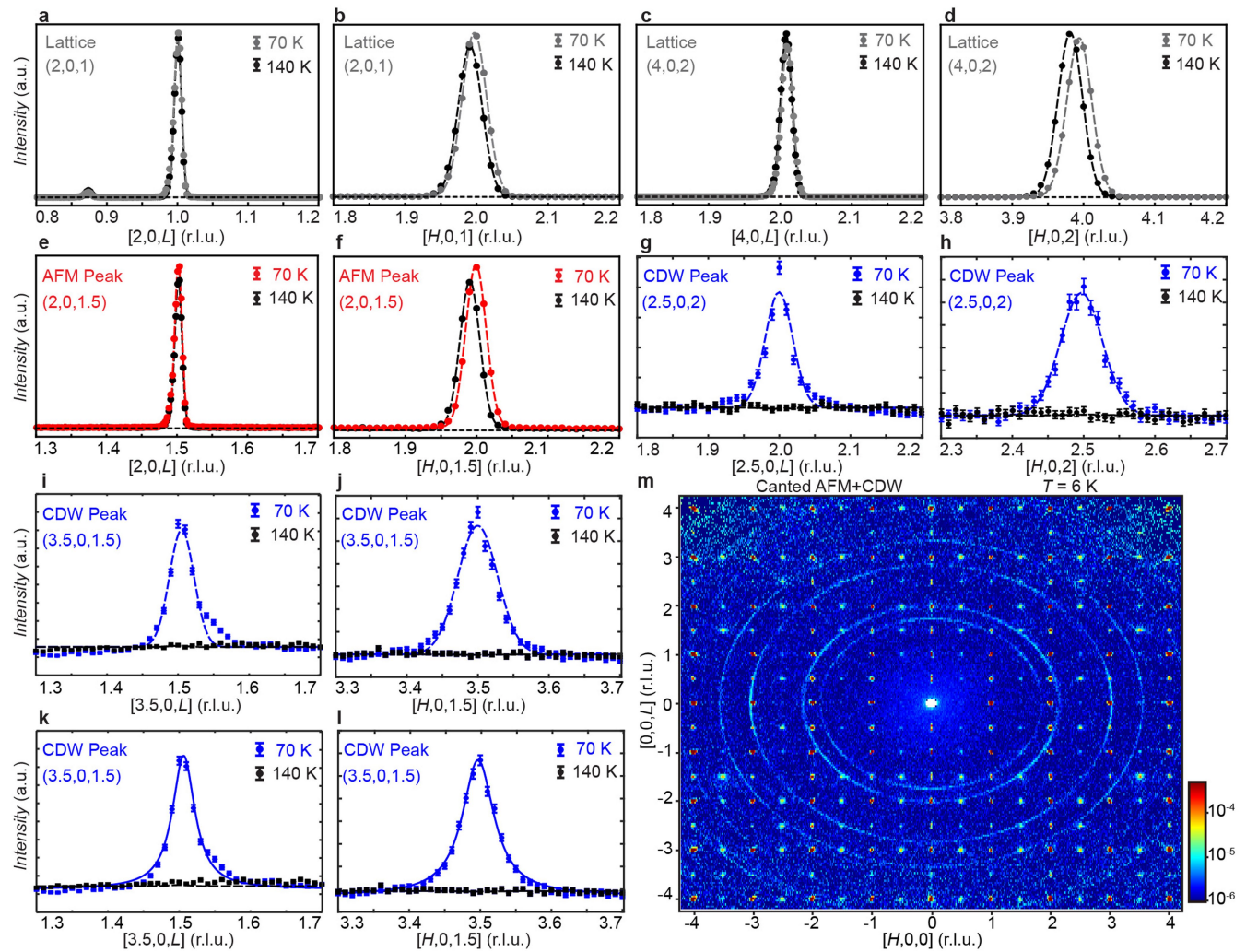
temperature. At T_{CDW} (100 K), the χ_{\perp} curve begins to have a shoulder directly under the spin-flop field instead of a sharp spin-flop transition. **c**, Magnetic moment at different temperatures and fields. Dashed lines are phase boundaries. **d**, Heat capacity versus temperature. A kink is observed at T_{CDW} .



Extended Data Fig. 3 | Electron density, electron mobility and Hall resistivity at various temperatures and fields. **a,b**, Field dependence of Hall resistivity ρ_{xy} at various temperatures. The step-like feature at high field that corresponds to spin-flop transition becomes less prominent below T_{CDW} (100 K) but is present nevertheless. **c**, Red dots show the electron density n_e versus temperature (left axis). With decreasing temperature, a sudden decrease is

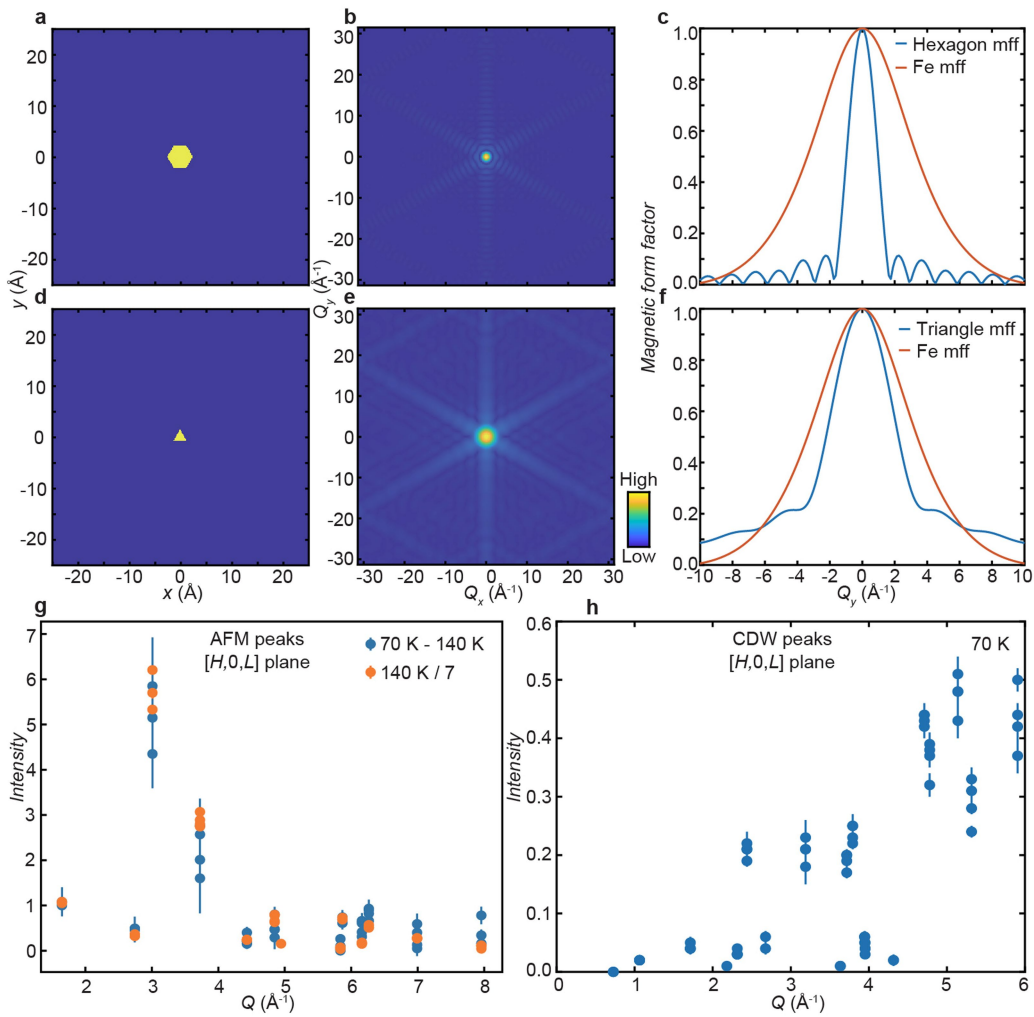
observed at T_{CDW} . Blue dots show the electron mobility μ_e versus temperature. An increase in slope occurs at T_{CDW} . **d,e**, Colour plot of ρ_{xy} and $d\rho_{xy}/dB$ at different temperatures and fields. Spin-flop transition becomes less clear below T_{CDW} . **f**, Temperature dependence of $d\rho_{xy}/dB$ for fields above and below spin-flop transition. **g,h**, The absence of hysteresis in ρ_{xy} , either below ($T = 10 \text{ K}$) or above ($T = 120 \text{ K}$) the T_{CDW} .

Article



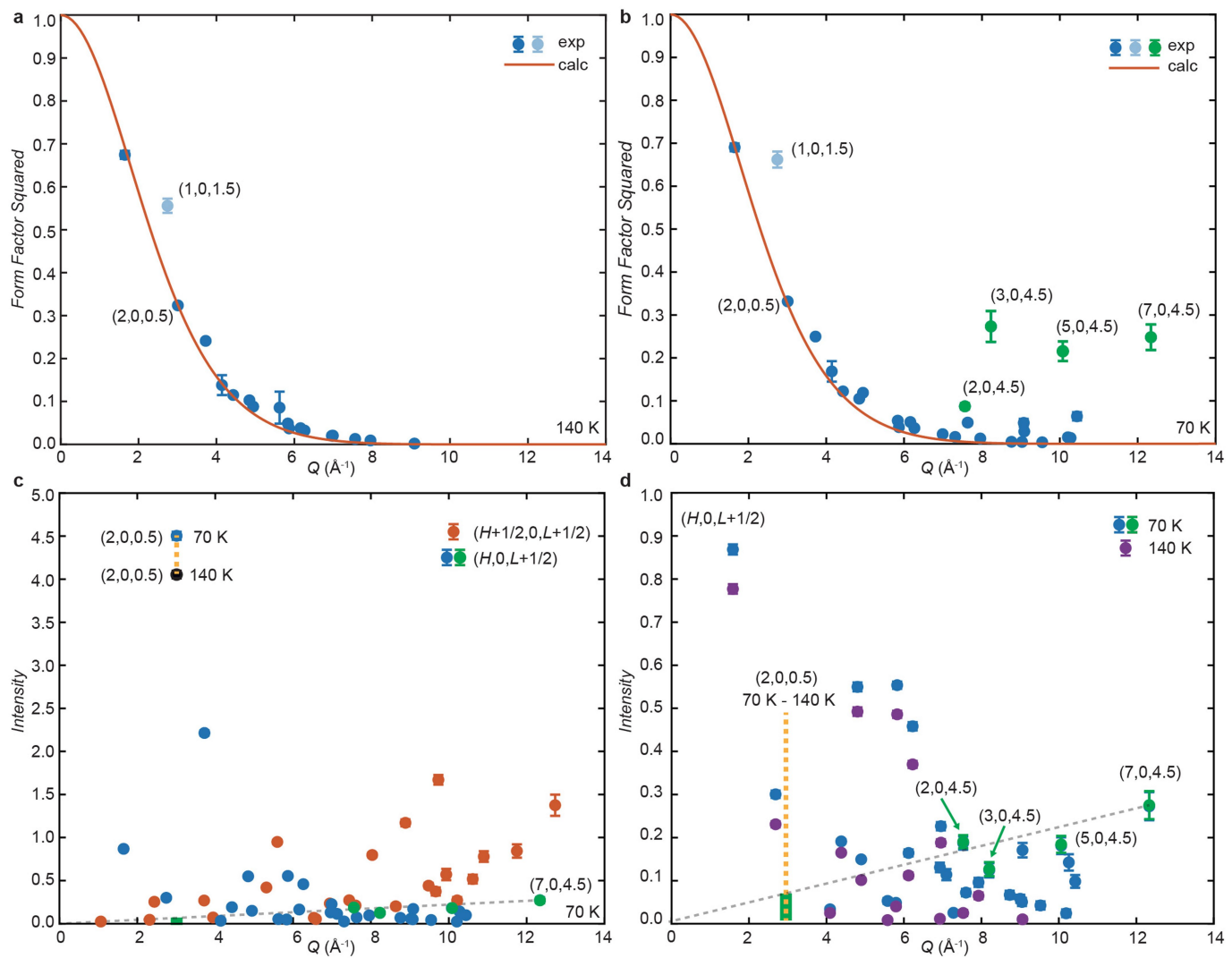
Extended Data Fig. 4 | Line shape of selected lattice, magnetic and CDW peaks and neutron diffraction map at 6 K. Cuts of lattice peak (2, 0, 1) (a, b), (4, 0, 2) (c, d), AFM magnetic peak (2, 0, 1.5) (e, f), CDW peak (2.5, 0, 2) (g, h) and CDW peak (3.5, 0, 1.5) (i–l) along the L and H directions, respectively.

Integration range is ± 0.1 r.l.u. Black dots are 70-K data. Grey, red and blue dots are 140-K data. Dashed lines in panels a–j are Gaussian fits and solid lines in panels k and l are Lorentzian fits. m, $[H, 0, L]$ plane map is taken at 6 K, in canted AFM + CDW phase. Clear CDW peaks at $\mathbf{Q}_{\text{CDW}1} = (0.5, 0, 0.5)$ and $\mathbf{Q}_{\text{CDW}2} = (0.5, 0, 0)$ are observed.



Extended Data Fig. 5 | Form factors of the flux phase, magnetic and CDW peaks. **a**, A flux hexagon in the real space. **b**, The 2D Fourier transform of the hexagon. **c**, A cut along Q_y in **b** with $Q_x = 0$, showing the magnetic form factor of the flux hexagon, with a comparison of the magnetic form factor of Fe atom. **d–f**, The flux triangle in the real space, its Fourier transform and the form factor along the $[0, Q_y]$ direction compared with Fe magnetic form factor,

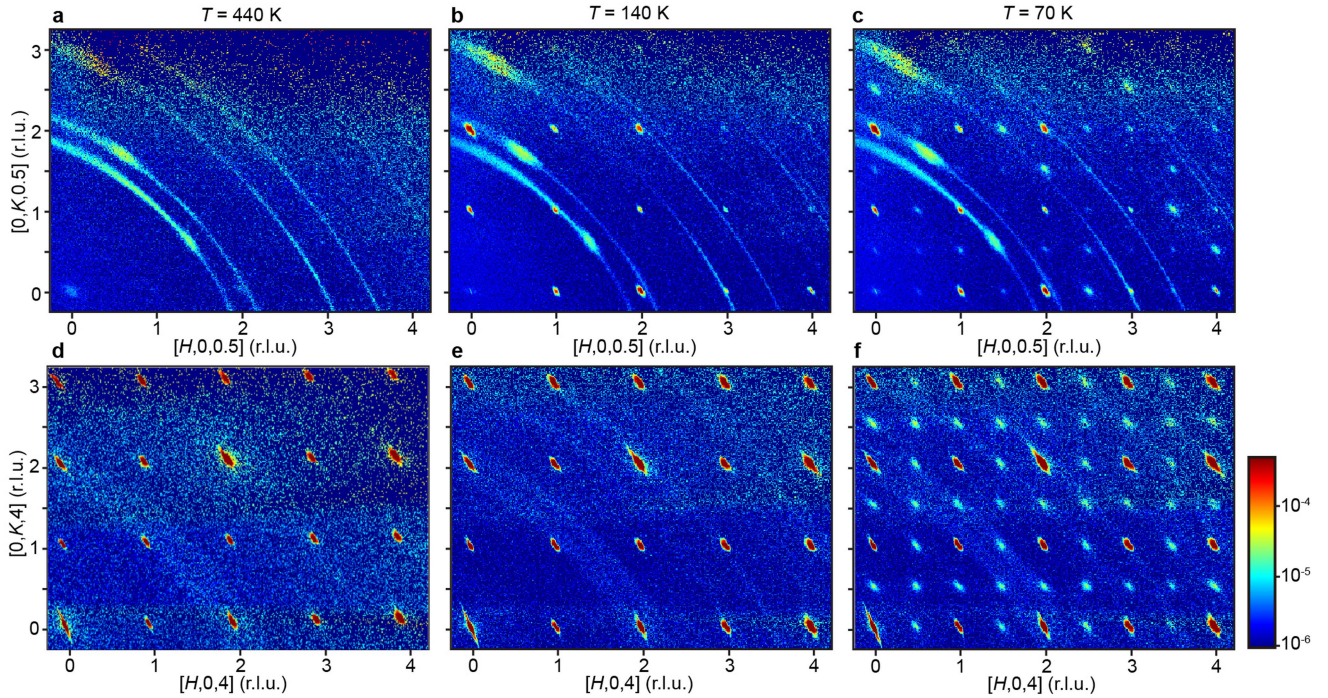
respectively. **g**, Wavevector dependence of the magnetic Bragg peak intensity in the $[H, 0, L]$ plane at 140 K and the extra intensity induced by CDW (calculated by subtracting 140 K intensity over 70 K). The CDW-induced intensity shows similar Q dependence as Fe atom. **h**, Wavevector dependence of the CDW peak intensity in the $[H, 0, L]$ plane at 70 K.

**Extended Data Fig. 6 | Estimation of lattice components on the magnetic**

Bragg peak positions. **a**, Comparison of integrated scattering intensity at all $(H, 0, L+1/2)$ magnetic Bragg peak positions at 140 K after accounting for the A-type AFM structural factor but not the magnetic form factor.

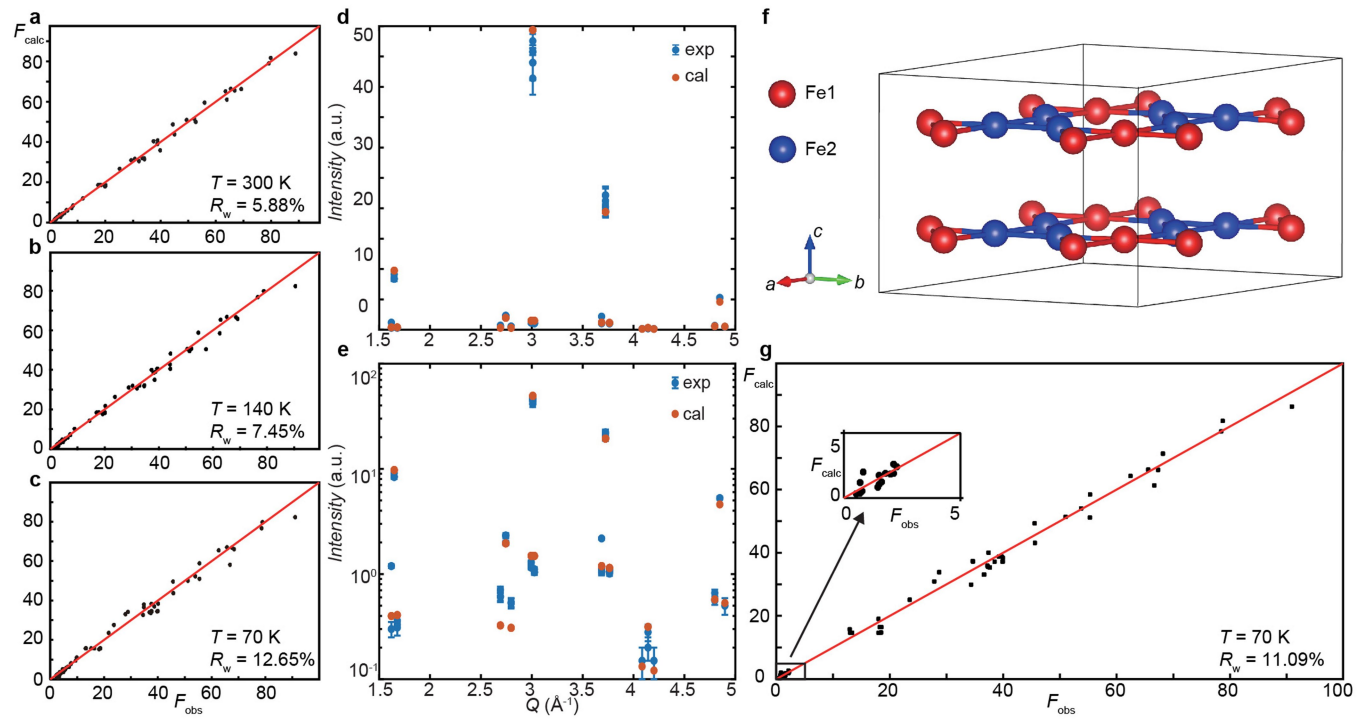
b, Integrated intensity at all $(H, 0, L+1/2)$ magnetic Bragg peak positions at 70 K. The orange solid lines in **a** and **b** are Fe magnetic form factors discussed in Extended Data Fig. 5. Green dots highlight unexpected Bragg peak positions that deviate from the Fe magnetic form factor (orange lines). White-shaded blue dots indicate Bragg peaks markedly contaminated with aluminium powder ring. **c**, Comparison between the integrated scattering intensity

at all $(H, 0, L+1/2)$ magnetic (blue, green) and superlattice $(H+1/2, 0, L+1/2)$ (orange) Bragg peak positions at 70 K. These are raw data without any correction and, thus, should be the most accurate description of the scattering intensity at both positions. The integrated intensity of the $(2, 0, 0.5)$ peak at 140 K is shown in the solid black circle. The solid green circles indicate anomalous data at $(H, 0, 4.5)$ positions. **d**, Expanded view of integrated scattering intensity at $(H, 0, L+1/2)$ positions at 70 K (blue, green) and 140 K (purple). The green bars in **c** and **d** near 3 \AA^{-1} indicate the estimated lattice component at $(2, 0, 0.5)$, if present, compared with the intensity gain between 70 K and 140 K shown in the dashed yellow lines.



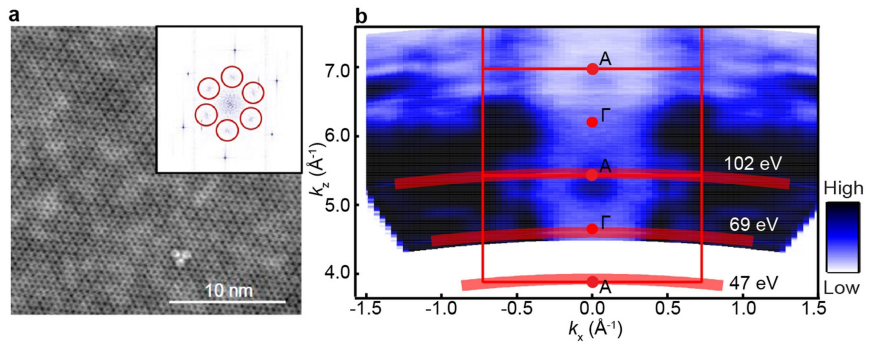
Extended Data Fig. 7 | $[H, K, 0.5]$ plane neutron diffraction maps at various temperatures. **a–c**, $[H, K, 0.5]$ plane diffraction maps at 440 K, 140 K and 70 K, respectively. At 440 K ($T > T_N$), no magnetic peak is observed; at 140 K ($T_{CDW} < T < T_N$), AFM peaks emerge at $H, K = 1, 2, 3, \dots$; At 70 K ($T < T_{CDW}$), further

CDW peaks emerge at $H, K = 0.5, 1.5, 2.5, \dots$. **d–f**, $[H, K, 4]$ plane diffraction maps at 440 K, 140 K and 70 K, respectively. Colour bar is in log scale. At 440 K ($T > T_N$) and 140 K ($T_{CDW} < T < T_N$), structural peaks are present at $H, K = 1, 2, 3, \dots$; at 70 K ($T < T_{CDW}$), CDW peaks emerge at $H, K = 0.5, 1.5, 2.5, \dots$



Extended Data Fig. 8 | Structure refinement results and possible lattice distortion for CDW order. **a–c**, The refinement result on lattice and magnetic Bragg peaks at 300 K, 140 K and 70 K, respectively. **d,e**, Comparison of calculated and experimental magnetic peak intensity in the incommensurate

phase at 6 K. **f**, Schematic diagram of the crystal structure of FeGe with two independent iron positions plotted. **g**, Refinement results using a simple model discussed in Methods.



Extended Data Fig. 9 | Extended STM and ARPES data. **a**, STM topographic data taken at $V = -30$ mV and $I = 0.1$ nA. The inset shows its Fourier transform, in which the red circles mark the 2×2 CDW vector peaks. **b**, Photon-energy-dependent ARPES measurement of FeGe. Electron-like pockets are observed at

A points. Inner potential is determined to be 16 eV. Thick red lines mark out in-plane high-symmetry cuts at various photon energies: $h\nu = 69$ eV corresponds to $k_z = 0$ (Γ -K-M); $h\nu = 47$ eV and 102 eV correspond to the $k_z = \pi$ plane (A-H-L). Measurement is performed at 8 K.

Article

Extended Data Table 1 | Crystal data and structure refinement for FeGe

Density (calculated)	7.344 g/cm ³
Absorption coefficient	36.6 mm ⁻¹
F(000)	58
Crystal size	0.100 x 0.100 x 0.100 mm ³
Theta range for data collection	4.722 to 33.062°.
Index ranges	$-7 \leq H \leq 7, -7 \leq K \leq 7, -6 \leq L \leq 6$
Reflections collected	4577
Independent reflections	92 [R(int) = 0.0456]
Completeness to theta = 25.242°	100.0 %
Refinement method	Full-matrix least-squares on F ²
Goodness-of-fit on F ²	1.136
Final R indices [I>2sigma(I)]	R1 = 0.0346, wR2 = 0.0866
R indices (all data)	R1 = 0.0346, wR2 = 0.0866
Extinction coefficient	0.040(12)

The measurements were carried out at 150(1)K. FeGe has a formula weight of 128.4. The X-ray wavelength is 0.71073 Å. Crystal structure is hexagonal with space group P6/mmm. The unit cell dimensions are $a=4.98493(11)$ Å, $b=4.98493(11)$ Å, $c=4.04911(10)$ Å, $\alpha=90^\circ$, $\beta=90^\circ$ and $\gamma=120^\circ$, resulting in a unit cell volume of $87.138(4)$ Å³.

Extended Data Table 2 | Atomic positions of FeGe

	x	y	z	Occupancy	U(eq)
Ge(1)	0	0	0	0.94	6(1)
Ge(2)	3333	6667	5000	1.00	4(1)
Fe(1)	5000	0	0	1.00	4(1)

Atomic (coordinates $\times 10^4$) and equivalent isotropic displacement parameters ($\text{\AA}^2 \times 10^3$) for FeGe at 150 K. $U(\text{eq})$ is defined as one-third of the trace of the orthogonalized U^{ij} tensor.

Article

Extended Data Table 3 | Atomic displacement factors

	U^{11}	U^{22}	U^{33}	U^{23}	U^{13}	U^{12}
Ge(1)	3(1)	3(1)	10(1)	0	0	2(1)
Ge(2)	5(1)	5(1)	4(1)	0	0	2(1)
Fe(1)	3(1)	3(1)	4(1)	0	0	1(1)

Anisotropic displacement parameters ($\text{\AA}^2 \times 10^3$) for FeGeat 150 K. The anisotropic displacement factor exponent takes the form: $-2\pi^2[h^2a^{*2}U^{11} + \dots + 2hka^*b^*U^{12}]$.

Extended Data Table 4 | Positions of atoms in the CDW phase of FeGe

Atom	X	y	z
Fe1	0.2500	0	0.2567
Fe2	0.5000	0.2500	0.2522
Ge1	0	0	0.2500
Ge2	0.5000	0	0.2500
Ge3	0.3333	0.1667	0.5000
Ge4	0.3333	0.6667	0.5000
Ge5	0.1667	0.3333	0.0000
Ge6	0.3333	0.6667	0.0000

The refinement is carried out using the structural superlattice peaks and assume non-ideal positions for the Fe atoms.